DESIGN AND MODELING OF A LARGE PROTON EXCHANGE MEMBRANE
FUEL CELL WITH HIGH HYDROGEN UTILIZATION FOR AUTOMOTIVE
APPLICATIONS

by
OMID BABAIE RIZVANDI

Submitted to the Graduate School of Engineering and Natural Sciences
in partial fulfillment of
the requirements for the degree of
Master of Science

Sabanci University

Design and Modeling of a Large Proton Exchange Membrane Fuel Cell with
High Hydrogen Utilization for Automotive Applications
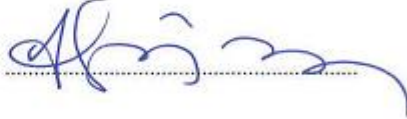
APPROVED BY:

Prof. Dr. Serhat Yeşilyurt
(Thesis Supervisor)

Assoc. Prof. Dr. Selmiye Alkan Gürsel

Asst. Prof. Dr. Mustafa Fazıl SERİNCAN

DATE OF APPROVAL: 4/8/2016

ABSTRACT

DESIGN AND MODELING OF A LARGE PROTON EXCHANGE MEMBRANE FUEL CELL WITH HIGH HYDROGEN UTILIZATION FOR AUTOMOTIVE APPLICATIONS

OMID BABAIE RIZVANDI

MSc. Thesis,

Thesis Advisor: Prof. Dr. Serhat Yeşilyurt

Keywords: Proton exchange membrane fuel cell, Flow field design, Species transport, Dead-ended operation, Ultra-low stoichiometric flow condition.

Performance of proton exchange membrane fuel cell (PEMFC) depends on several factors, such as flow fields design, cooling technique, species transport, and water management. In order to enhance the performance of a high power (automotive) PEMFC, three-dimensional model of the anode flow field with ultra-low stoichiometric flow condition and without the effect of species transport, two-dimensional model of the anode flow field with species transport, and three-dimensional serpentine flow fields for the cathode and cooling domains are studied and optimized. In the anode models, widths of the channels and ribs and configurations of their headers are investigated to obtain a uniform flow and hydrogen concentration distribution through the channels. For the anode flow field, two approaches lead to different optimum designs, however, we prefer the one from the two-dimensional model with the mass transport. In the final design of the anode flow field, the hydrogen-depletion region ratio is less than 0.2%. In the cathode model, an unstructured search is used to obtain a design that has a pressure drop within 30% of the output power. In the cooling model, dimensions of the channels and ribs, and pressure difference between the inlet and outlet manifolds are investigated to find a uniform temperature distribution through the cooling plate with index of uniform temperature (IUT) less than 3 °C. Finally, a one-dimensional model of species and liquid water transport and distribution through the anode and cathode channels and their gas diffusion layers (GDLs) is studied. Results of this model agree reasonably with experimental data.

ÖZET

OTOMOTİV UYGULAMARI İÇİN YÜKSEK HİDROJEN KULLANIMLI GENİŞ BİR PROTON DEĞİŞİM MEMBRANLI YAKIT HÜCRESİNİN TASARIMI VE MODELLEMESİ

OMID BABAIE RIZVANDI

Yüksek Lisans Tezi,

Tez Danışmanı: Prof. Dr. Serhat Yeşilyurt

Anahtar kelimeler: Proton değişim membranlı yakıt hücresi, Akış alanı tasarımı, Bileşenlerin taşınımı, Ölü-sonlu çalışma, Çok-düşük stokiyometrik akış koşulu.

Proton değişim membranlı yakıt hücresinin (PDMYH) performansı akış alanı tasarımı, soğutma tekniği, bileşenlerin taşınımı ve su yönetimi gibi birkaç etkene bağlıdır. Yüksek güçlü bir (otomotiv) PDMYH'nin performansını artırmak için, çok-düşük stokiyometrik akış koşuluyla ve bileşenlerin taşınımının etkisi olmadan üç-boyutlu bir anot akış alanı modeli, bileşenlerin taşınımıyla iki-boyutlu bir anot akış alanı modeli ve katot ve soğutucu alanları için üç-boyutlu serpantin akış alanları çalışılmış ve optimize edilmiştir. Anot modellerinde, kanallarda üniform bir akış ve hidrojen yoğunluk dağılımı elde etmek için kanalların ve kaburgaların genişlikleri ile bunların başlıklarının biçimleri incelenmiştir. Anot akış alanı için izlenen iki yaklaşım farklı optimum tasarımlarla yol açmaktadır, fakat biz iki-boyutlu kütle taşınımlı modelden geleni tercih ediyoruz. Nihai anot akış alanı tasarımında, hidrojen-tükenimi bölgesi oranı %0.2'den azdır. Katot modelinde, basınç düşümü çıkış gücünün %30'u içerisinde olacak bir tasarım elde etmek için yapısal olmayan bir arama kullanışmıştır. Soğutma modelinde, soğutma paneli üzerinde üniform sıcaklık indeksi 3'ten az bir üniform sıcaklık dağılımı bulmak için kanal ve kaburgaların boyutları ve giriş ve çıkış manifoldları arasındaki başınç farkı incelenmiştir. Son olarak, anot ve katod kanalları ile bunların gaz difüzyon takabaları aracılığıyla bileşenler ve sıvı suyun taşınımı ve dağıtımı için bir-boyutlu bir model üzerinde çalışılmıştır. Bu modelin sonuçları deneysel verilerle makul ölçüde uyuşmaktadır.

… to my wife

ACKNOWLEDGMENTS

I would like to express my sincere gratitude and appreciation to my advisor Professor Dr. Serhat Yeşilyurt for his continuous support in all the time of research and writing of this thesis. I would like to thank him for his patient, motivation, encouragement, and all of the opportunities that he has provided me. I would also like to thank my committee members, Associate Professor Selmiye Alkan Gürsel and Assistant Professor Mustafa Fazıl SERİNCAN for serving as my committee members and their insightful comments and suggestions.

I would like to thank my beloved wife Hana for supporting me spiritually. Words cannot express how grateful I am to her.

TABLE OF CONTENTS

LIST OF FIGURES

LIST OF TABLES

LIST OF SYMBOLS AND ABBREVIATIONS

C_p	Heat capacity at constant pressure
d_1	Half of the length of the central segment in the feed header
d_2	The length of the side segments in the feed header
d_{cb}	The length of the central baffle
F	Faraday's constant
h_w	Thickness of the water channels
$J_{loss,0}$	Current density loss constant
k	Thermal conductivity
K_{cond}	Condensation coefficient
K_{evap}	Evaporation coefficient
K_m	Membrane permeability
K_0^l	Intrinsic permeability of the GDL
L	Length of the channels
n	Number of baffles in the inlet header
n_{chc}	Number of the cathode channels
n_{chw}	Number of the water channels
N_{ch}	Number of the anode channels
n_d	Electro-osmotic drag coefficient
P	Pressure
P_0	Reference pressure

q	Heat flux
Q	Heat
R	Universal gas constant, reaction rate
Re	Reynolds number
R_{solid}	Electric resistance of the solid part of the cell
S	Liquid water saturation
T	Temperature
T_0	Reference temperature
u	Velocity vector
$\bar{V}_{ch}$	Average of the centerline velocities
$V_{ch,k}$	Centerline velocity of the kth channel
V_{max}	Maximum velocity of the fluid in the channels
V_m	Molar volume of the membrane
v_{H_2}	Molar volume of hydrogen
v_{N_2}	Molar volume of nitrogen
w_{ch}	Width of the anode channels
w_{chc}	Width of the cathode channels
w_{chw}	Width of the water channels
w_{gap1}	Widths of the gaps between the segments in the feed header
w_{rib}	Width of the anode ribs
w_{rc}	Width of the cathode ribs
w_{rw}	Width of the water ribs
w_{gb}	Widths of the gaps between the baffles
w_{gs}	Widths of the side gaps

$c_{SO_3}^{0}$ Concentration of sulfonic in the membrane

$c_{\{H_2,O_2\}}^{ref}$ Reference concentrations of H_2 and O_2

$i_{0,ref}^{(an,ca)}$ Reference current density at the anode and cathode

$x_{N_2,ca}$ Molar fraction of nitrogen in the cathode

Greek letters

∇ Vector differential operator

δ_m Thickness of the membrane

δ_{gdl} Thickness of the GDL

ρ Density

μ Dynamic viscosity

ν Kinematic viscosity

ε Porosity of the GDL

Φ_1 Root mean square (rms)

Φ_2 Ratio of maximum and minimum values of the channel average velocities

Φ_3 Area fraction

$\psi_{N_2,0}$ Reference permeance coefficient of nitrogen

γ_{H_2} Concentration coefficient of hydrogen

γ_{O_2} Concentration coefficient of oxygen

$\beta_{\{an,ca\}}$ Transfer coefficients of the anode and cathode sides

$\lambda_{\{an,ca,m\}}$ Water content in the anode, cathode, and membrane

Abbreviation

BP   Bipolar plate

CFD   Computational fluid dynamics

CL   Catalyst layer

DEA   Dead-ended anode

EH   Exhaust header

FH   Feed header

GDL   Gas diffusion layer

IM   Inlet manifold

IUT   Index of uniform temperature

MPL   Micro porous layer

MSP   Method of standard porosimetry

OM   Outlet manifold

PEM   Proton exchange membrane or polymer electrolyte membrane

PEMFC   Proton exchange membrane fuel cell

ULS   Ultra-low stoichiometry

ULSFC   Ultra-low stoichiometry flow condition

1. INTRODUCTION AND LITERATURE REVIEW

Proton exchange membrane fuel cell (PEMFC) is one of the most promising alternative energy conversion device which converts the chemical energy to the electrical energy directly and efficiently. Its high power density, low-temperature operation (< 100 °C), fast start-up time, low emissions, and system robustness advantages have ensured that it becomes one of the most favorable power sources for the majority of motor manufacturers [1-4]. In spite of considerable development and research of the PEM fuel cells, there are barriers to their commercialization due to their durability and cost [4-5].

Components of a typical PEM fuel cell are: a solid membrane, bipolar plates with flow field channels on each side of the cell (anode and cathode sides) for reactant distribution, gas diffusion layers (GDLs) on the bipolar plates, and catalyst layers (CLs) on each side of the membrane, as shown in Fig. 1.1. Hydrogen is supplied to the anode flow field, distributed through the anode channels, then it diffuses into the anode GDL, and then into the anode CL. Oxygen (typically air) is supplied to the cathode flow field, distributed
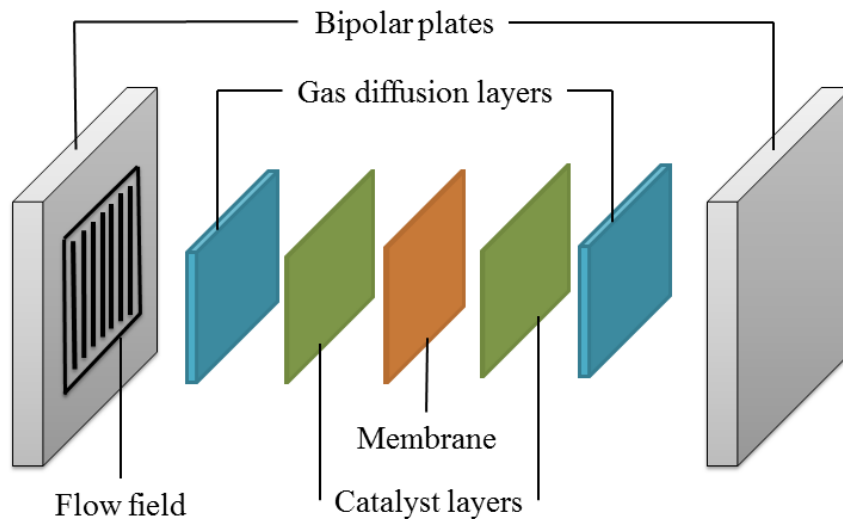
FIGURE 1.1: Components of a typical PEM fuel cell.

1

through the cathode channels, then it diffuses into the cathode GDL, and then into the cathode CL. Hydrogen is divided into proton and electron at the anode CL. The protons go to the cathode side through the membrane and electrons go through an external circuit and produces electrical power. Membrane conducts protons while it is not permeable to electrons and hydrogen and oxygen gases. Oxygen reacts with the protons and electrons come from the anode side, and this reaction produces water and heat since the reaction is exothermic. The generated water and heat are by-products, some portion of this water is needed to enhance the conductivity of the membrane and its excess amount and the generated heat must be removed effectively. Reactions at the anode and cathode sides and overall reaction are as follows:

Anode reaction (oxidation): $2H_2 \rightarrow 4H^+ + 4e^-$

Cathode reaction (reduction): $O_2 + 4H^+ + 4e^- \rightarrow 2H_2O$

Overall cell reaction: $2H_2 + O_2 \rightarrow 2H_2O + Heat$
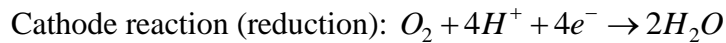
A representative schematic of PEM fuel cell is shown in Fig. 1.2.

A complete model of PEM fuel cell is complicated since it involves heat transfer, species and charge transport, electrochemical reactions, structural, and multiphase flow
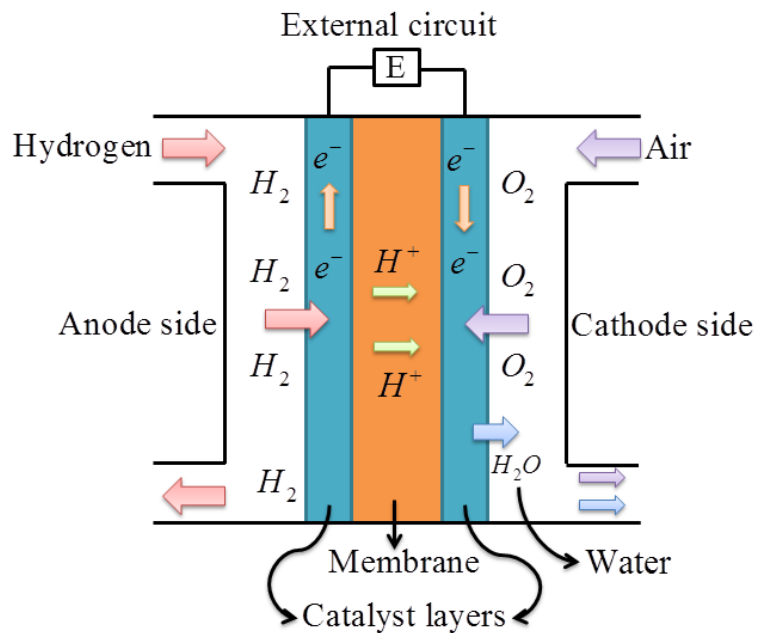
FIGURE 1.2: Schematic of a PEM fuel cell.

2

analysis. Therefore, appropriate mathematical and numerical models with reasonable assumptions can be applied to the sub-models.

Bipolar plates (BPs) are one of the important components of PEM fuel cells. They supply and distribute the reactants through the active area uniformly, are used as electrical connectors between cells, remove heat from the cell, and prevent leakage of gases and cooling. Proper design of the BPs is essential since they take about 80% of the weight and 45% of the cost of PEM fuel cell stack [6]. A uniform flow distribution in the active area due to an efficient design of BPs can yield 50% increase in the output power [7].

There are several configurations can be used for flow fields on the BPs, such as pin-type, parallel channels, serpentine channel(s), integrated, and interdigitated flow fields [8]. Here, parallel channels flow field is used for the anode side and serpentine channels flow field is utilized for the cathode and cooling sides.

The configuration of the anode side includes straight parallel channels between the feed and exhaust headers. Straight channels with no directional changes yields to low pressure drop along the channels and between the inlet and outlet manifolds. This low pressure loss causes maldistribution of the flow (hydrogen) through the anode channels. The most common solution to this problem is using an appropriate arrangement of the baffles (constraints) in the feed and exhaust headers.

A typical operation in the anode side is dead-ended anode (DEA), which utilizes periodic purges at the anode exit by means of a passive capillary valve or a high-speed purge valve. This operation reduces the intricacy of the design of the PEMFC and it has some disadvantages, such as nitrogen and liquid water accumulation in the anode flow field (blanketing phenomena) which results in hydrogen starvation spots (regions) in the anode active area, increases the current density of the not starved regions of the anode active area, severe voltage transients, and carbon corrosion at the CLs [9-11]. In sections 2.1 and 2.2, an alternative operation which is ultra-low stoichiometric (ULS) flow condition is applied to the anode flow. In this approach, the anode exit velocity is specified based on the permeance of nitrogen to the anode side and objective is to obtain a uniform flow distribution through the anode channels.

Maharudrayya et al. [12] studied one-dimensional steady model of the Z and U-type parallel channel configurations. Authors investigated the effect of the channels dimensions

and configurations of the feed and exhaust headers on the uniformity of the flow distribution in the channels. For the assessment of the uniformity of the flow distribution, they used two performance metrics as the normalized difference between the maximum and minimum flow rates of the channels, and the rms (root mean square) of these flow rates. They reported that uniformity of the flow can be improved efficiently by an appropriate design of the feed and exhaust headers as well as channels geometries. Kee et al. [13] studied one-dimensional channel network model of the flow distribution in the solid oxide fuel cells. Authors illustrated the importance of the effect of the pressure distribution in the headers on the uniformity of the flow distribution through the channels; similar study was done by [12]. Wei et al. [14] developed an evolutionary algorithm to optimize the configuration of the baffles in the feed and exhaust headers of the flow field for uniform flow distribution through the channels. Jackson et al. [15] studied a network model of the flow distribution of the Z-type channel configurations. They demonstrated that typical maldistribution occurs in the middle channels, which can be improved to a uniform flow distribution in the channels by increasing the widths of the feed and exhaust headers.

In sections 2.1 and 2.2, the anode domain consists of parallel channels, feed and exhaust headers, and inlet and outlet manifolds are considered. Boundary conditions are specified as a constant pressure at the inlet manifold and a constant velocity or flow rate at the outlet manifold. An unstructured approach is used to obtain a uniform flow distribution in the channels instead of structured optimization methods, and whenever the configuration is fixed a grid-search is employed over the range of the design parameters. In section 2.1, the species transport through the membrane and reactions are neglected while they are included in the model presented in section 2.2.

In order to overcome the problems of the straight channels, especially low pressure drop and flow maldistribution, serpentine channel flow fields are developed [16]. Serpentine flow fields are common for the cathode side since higher pressure differences between the inlet and outlet manifolds are needed to remove the generated water at the cathode side. Therefore, the most important design goal of the cathode configuration is to obtain a certain amount of pressure drop through the channels from the inlet manifold to the outlet manifold. This pressure drop must be high enough to push the water droplets, which are formed in the cathode channels, to the cathode exit and it must be low enough to reduce

the parasitic power, which is supplied to the compressor to pressurize the inlet air, and subsequently to enhance the cell efficiency.

Watkins et al. [7] suggested a single serpentine channel for the flow field which connects to the inlet and outlet manifolds from its ends. This design yields a long path of the reactants flow which results in significant pressure loss and considerable flow gradients between the inlet and outlet manifolds. Furthermore, the water flooding (blockage) is possible in this design, since all water droplets are formed and accumulated in a single channel and more power is needed to remove them from the channel. Authors found that by using some parallel serpentine channels the mentioned disadvantages of a single serpentine channel can be improved [17]. By changing the number of the serpentine channels, the desired pressure drop can be achieved. They claimed that the performance of the cell can be increased 50% by using serpentine channels for the flow field. In a similar study, Li et al. [8] studied serpentine flow fields with the active areas of 50, 100, 200, 300, and 441 cm^2. Authors reported that using serpentine channels enhance the performance of the cell since they remove the liquid water formed in the cell effectively. Their results of the neutron imaging technique indicate no liquid water in the cell for the mentioned cases.

In section 2.3, the cathode domain consists of the parallel serpentine channels, and its inlet and outlet manifolds are considered. Boundary conditions are specified as a constant mass flow rate at the inlet manifold and a constant pressure at the outlet manifold. An unstructured approach is used to find a sufficient number of the channels and consequently adequate pressure drop from the inlet to the outlet to remove the liquid water from the cell, minimize the parasitic power of the cell, and minimize the concentration gradients of the flow from the inlet manifold to the outlet manifold.

Using an efficient cooling technique is essential for effective operation of the high power (automotive) PEM fuel cell stacks. The generated heat at the stack due to the exothermic reactions at the cathode sides of the cells must be removed to prevent overheating of the membrane and catalyst layers (CLs). The operation temperature of the membrane of the low-temperature PEM fuel cell is from 60 to 80 °C, and higher temperatures can increase the degradation of the membrane as well as the catalyst layers and consequently reduce the efficiency of the stack [18-19]. Heat removal by means of the reactants flow, especially air at the cathode side since its stoichiometric ratio is high and it

takes part in the exothermic reaction, and the generated water stream is very low and negligible, hence external cooling system must be used for the high power PEM fuel cell stacks [20]. Utilizing an external cooling system increases the parasitic power, weight, and cost of the PEM fuel cell stack and consequently it reduces the performance of the stack [21].

Some of the cooling techniques used in the PEM fuel cell stacks are: cooling with liquids such as water, cooling with separated air flow, cooling by increasing the amount of air flow supplied to the cathode side, cooling with phase change, and cooling with heat spreaders such as high thermal conductivity materials and heat pipes [2-3 and 22-23]. Cooling with the liquid water, which has a very high heat capacity, is the most common method used in the high power (automotive) PEM fuel cell stacks [24-25]. The number of the cells comes between two adjacent cooling layers is an important parameter in the design of the cooling system, and it is proved that it has an inverse effect on the stack performance [26].

Chen et al. [27] developed a thermal analysis to optimize the configuration of the cooling flow field of a PEM fuel cell stack. They analyzed straight channels and serpentine type flow field configurations and compared their results. They reported that cooling effects of the serpentine type flow fields is better than parallel channel flow fields, however, the parasitic power of the parallel channel flow fields are less than serpentine flow fields. Similar results were found by Choi et al. [28].

In section 2.4, the cooling domain consists of the parallel serpentine channels, and the inlet and outlet manifolds are considered. Boundary conditions are specified as constant pressures at the inlet and outlet manifolds, a constant temperature at the inlet manifold, and a constant heat flux on the active area of the cooling plate. Effects of the number of the channels and their dimensions, the dimensions of the ribs, and the pressure difference applied to the inlet and outlet manifolds are investigated and optimized to obtain the final design of the cooling flow field. The objective of this study is to design a cooling flow field configuration which its value of the index of uniform temperature (IUT), which is defined as the difference between the maximum and minimum temperatures over the plate of the cooling flow field, be less than 3 °C.

6

In a common PEM fuel cell operation, humidified hydrogen is supplied to the anode inlet and humidified oxygen is provided to the cathode inlet. These species are distributed in the anode and cathode channels by convection due to the convective velocity of the flow supplied to the anode and cathode inlets. Afterward, these species migrate to the catalyst layers (CLs) through the gas diffusion layers (GDLs) by diffusion and take part in the reactions at the CLs. Many mathematical and numerical models have been developed based on the transport phenomena in the components of the PEM fuel cells. Primary models were basic, highly simplified, one-dimensional, and concentrate on the transfer of species through the GDLs, CLs, and membrane [29-33]. Subsequently, two-dimensional models of the transport of the species and local current density in the PEM fuel cell components were developed, and computational fluid dynamic (CFD) was utilized to analyze the flow fields in the anode and cathode channels, GDLs, and CLs [34-37]. The next development is three-dimensional models of the PEM fuel cells by considering the conservation of mass, momentum, and species as well as the electrochemical reactions kinetics [38-43].

In section 2.2, a two-dimensional model of the anode domain consists of the parallel channels, and feed and exhaust headers is considered. In this model, nitrogen crossover and accumulation in the anode active area is investigated by means of Maxwell-Stefan equations coupled with a voltage model. Furthermore, water vapor is not included in the equations and constant values are used for the cathode side, i.e. the cathode side is not involved in this model. Performance metric used in this model is the hydrogen-depletion region ratio, which is defined as the ratio of the region contains the hydrogen mole fraction less than a value between 0 and 1 and the active area of the anode domain. The goal of this study is to design a configuration have a uniform distribution of the concentration of hydrogen in the anode active area while nitrogen is removed from the channels and hydrogen utilization is kept greater than 99%.

Water analysis is the most important issue in modeling and design of the PEM fuel cells. The water in the cell is a result of the humidified flows supplied to the anode and cathode inlets and generated water from the chemical reactions at the cathode side. Water exists in its liquid and vapor phases in the anode and cathode channels, GDLs, CLs, and membrane. Dissolved water is necessary for the transport of the protons through the membrane, and it is a barrier for the transport of the reactants through the anode and

7

cathode channels, GDLs, and CLs [44-46]. Great deals of mathematical and numerical models have been developed to analyze the two-phase flows and liquid water transport in the PEM fuel cells [47-53]. Neutron imagining technique is a powerful and nondestructive method to capture the distribution of liquid water in the components of the PEM fuel cell, and validate the results of the developed models [54-56].

The most important issue in modeling the liquid water distribution and transport through the components of the PEM fuel cells is the wettability behavior of the GDLs and CLs, which can be measured from their water-air capillary pressure curves. The water-air capillary pressure measurements are obtained by using the method of standard porosimetry (MSP) [57-60]. In this method, capillary pressure, which is defined as $P_C = P_L - P_G$, is measured as a function of the liquid water saturation in the GDLs and CLs. Gostick et al. [60] reported that negative capillary pressure yields the water withdrawal. Benziger et al. [61] reported that water injection is associated with the positive capillary pressures. Fairweather et al. [62] developed a method that investigated the capillary pressure for both injection and withdrawal of the water. Authors reported that the capillary pressure behavior as a function of the liquid water saturation show permanent hysteresis, and water withdrawal and injection are associated with the negative and positive capillary pressures, respectively. Similar results were reported for the capillary pressure versus the liquid water saturation by [63-64].

In section 2.5, a one-dimensional model of the anode and cathode channels and their GDLs are developed. In this model, species transport through the channels and GDLs are studied by solving Maxwell-Stefan equations coupled with a voltage model, which investigates the distribution of the current density and hydrogen consumption rate to obtain reactions kinetics. Further, phase change (evaporation and condensation) of the water and liquid water distribution and transport through the channels and GDLs are included in this model. Results of this model are compared with the experimental data provided by [65].

2. METHODOLOGY

2.1. Optimization of Flow Velocity Distribution through Anode Channels by Neglecting Species Transport

In this section, the goal is to design a flow field for the anode side of the cell. The model used here is a basic one, since species transport cross-over the membrane is neglected. Moreover, the objective of this study is to obtain a uniform flow distribution in the anode active area to ensure a uniform flow over the membrane.

A three-dimensional model of the flow velocity distribution in the anode flow field is developed. The anode flow field consists of the inlet and outlet manifolds, feed and exhaust headers, and parallel channels between headers, as demonstrated in Fig. 2.1.

Boundary conditions are specified as constant pressure and flow rate for the inlet and outlet manifolds, respectively. Exit flow rate is set to a low value (1.267×10^{-8} m^3/s) which is equal to the nitrogen permeance from the cathode side to prevent nitrogen accumulation (blanketing phenomena) in the anode channels. Accordingly, the Reynolds number of the flow in the channels is between 10^{-2} and 10^{-1}. The exit velocity must be set to a value that discharges the accumulated nitrogen and preserves the hydrogen and water vapor in the anode flow field.

2.1.1. Governing Equations

Reynolds number, which is a dimensionless number and used to characterize different flow regimes such as laminar or turbulent flows, is defined as:

$$\mathrm{Re} = \frac{\rho V_{\max} L}{\mu} = \frac{V_{\max} L}{\nu}$$

(1)

9
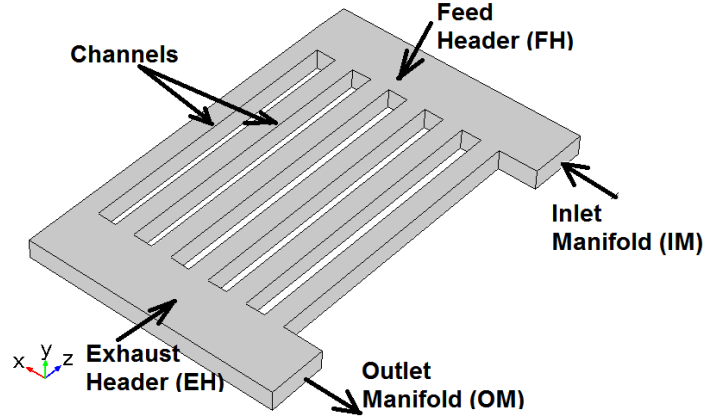
FIGURE 2.1: Representative geometry and components used for the anode flow field.

where V_{max} is the maximum velocity of the flow in the channels, L is the length of the channels, ρ is the density of the fluid, and μ and v are the dynamic and kinematic viscosity of the fluid, respectively. Since Reynolds number is low, Stokes (creeping) flow model is used for the flow in the anode flow field. Stokes equations are:

$$-\nabla p + \mu \nabla^2 \mathbf{u} = 0 \qquad (2)$$

where p is the pressure and $\mathbf{u}$ is the velocity vector. Further, continuity equation which refers to the incompressibility of the fluid (hydrogen) used is:

$$\nabla . \mathbf{u} = 0 \qquad (3)$$

These equations are utilized to analyze the flow in the anode flow field. Further, the inlet pressure and the outlet flow rate are set to 1.5 atm and 1.267×10^{-8} m^3/s. The no-slip boundary condition is used for the walls of the model domain.

2.1.2. Numerical Approach

In this study, modeling domain is anode channels and its inlet and outlet configurations. Stokes equations are applied to this domain by means of commercial finite element package, COMSOL Multiphysics [66].

10
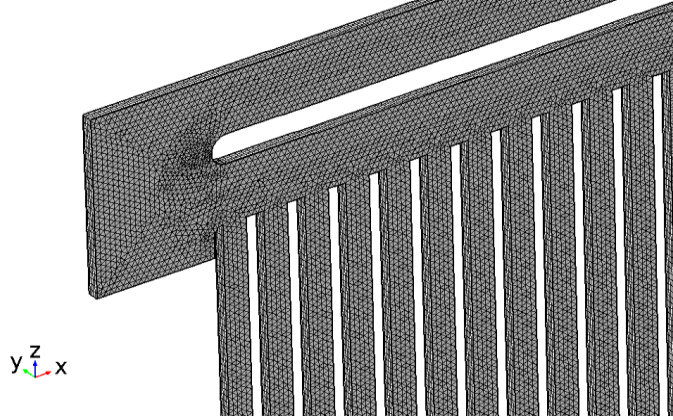
FIGURE 2.2: Distribution of typical finite-element mesh with 1157280 P1+P1 type prismatic elements and 3.2407×10^6 number of degrees of freedom.

A triangular mesh is used for the anode top surface and swept across the depth of the domain to obtain prismatic elements, as demonstrated in Fig. 2.2. The total number of degrees of freedom is about 3×10^6. The fully-coupled solution is used with Newton iterations and direct MUMPS solver. Pseudo time-stepping with an initial CFL condition of 5 is invoked.

2.1.3. Performance Metrics

Uniformity of the flow distribution in the anode channels is specified by two performance metrics. The first is the ratio of the maximum to minimum velocities in the channels:

$$\Phi_1 = \max_{1 \leq k \leq N_{ch}} \left\{ V_{ch,k} \right\} \Big/ \min_{1 \leq k \leq N_{ch}} \left\{ V_{ch,k} \right\} \tag{4}$$

where $V_{ch,k}$ is the centerline velocity of the kth channel and N_{ch} is the number of the channels of the model domain.

The second performance metric is the root-mean-square (rms) of the centerline velocities of the channels:

11

$$\Phi_2 = \left[\frac{\sum_{k=1}^{N_{ch}} \left(V_{ch,k} - \bar{V}_{ch} \right)^2}{N_{ch} \bar{V}_{ch}^2} \right]^{1/2} \tag{5}$$

Here, $\bar{V}_{ch}$ is the average of the centerline velocities of whole channels of the model. Similar metrics are used in literature for the assessment of the uniformity of the flow distribution in parallel channels. For example, in [12], authors used a performance metric for the rms-value of the channel flow rates, and the normalized range between the minimum and maximum flow rates.

2.2. Optimization of Flow Concentration Distribution through the Anode Active Area by Including Species Transport

In this section, a model which is more accurate than the model used in the previous section (2.1) is used to design a flow field for the anode side of the cell. In this study, species transport through the membrane is included in the analysis to obtain more realistic results.

A two-dimensional model of the nitrogen crossover and accumulation in the anode flow field is developed. Modeling domain consists of anode channels, inlet and outlet configurations, and gas diffusion layer (GDL), as demonstrated in Fig. 2.3. Since this model contains of species transport, GDL is included in the model as a connector between the channels (instead of ribs) and fills the baffles in the feed header. Hydrogen is supplied to the anode inlet manifold and as a result of its convective velocity nitrogen that passes through the membrane into the anode active area is pushed to the anode outlet manifold. Exit velocity is set to a low value equal to the nitrogen permeance from the cathode side times a coefficient and its value is varying between 10^{-3} and 10^{-2} m/s. Therefore, the Reynolds number of the flow in the channels is between 10^{-1} and 0. The exit velocity (leak rate) must be high enough to remove the nitrogen accumulated in the anode channels, and must be low enough to confine hydrogen and water vapor in the anode active area.
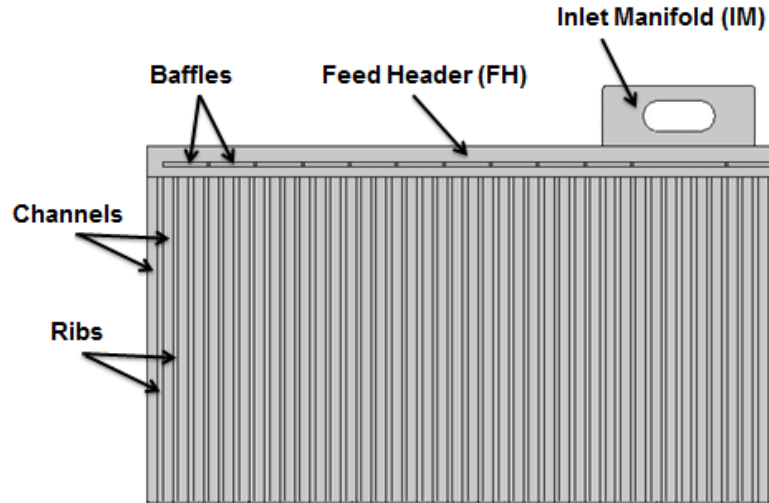
FIGURE 2.3: Anode channels and inlet configuration.

2.2.1. Governing Equations

Since Reynolds number is low, Stokes (Creeping) flow equations are used to model the flow distribution in the anode active area and its inlet and outlet configurations. Stefan-Maxwell equations are used to model the nitrogen and hydrogen transport and distribution in the modeling domain, resulting from both convection and diffusion. A voltage model is used to analyze the distributed current density and the hydrogen consumption rate, i.e. reactions kinetics. Values of the constants used in this model are listed in table 2.1.

2.2.1.1. Stokes flow

The analysis and equations used for the Stokes (Creeping) flow model in the anode flow field are similar to the ones used in the previous three-dimensional model of the anode flow field (section 2.1.1). The only difference is the outlet boundary condition, which is velocity in this model.

Table 2.1: Constants of Maxwell-Stefan and voltage models

Parameter	Value	Description
δ_m	50×10^{-6} m	Thickness of the membrane
L	0.16 m	Length of the channels
wch	2×10^{-3} m	Width of the channels
wrib	1×10^{-3} m	Width of the ribs
F	96,485 C/mol	Faraday's constant
T, T0	338 and 300 K	Operation and reference temperature
p, p0	1.5 and 1 atm	Operation and reference pressure
Vm	9×10^{-4} m^3/mol	Molar volume of the membrane
v_{N_2}	17.9×10^{-6} m^3/mol	Molar volume of nitrogen
v_{H_2}	7.07×10^{-6} m^3/mol	Molar volume of hydrogen
$c_{SO_3}^0$	1.2×10^3 mol/m^3	Concentration of sulfonic in the membrane
$\psi_{N_2,0}$	1×10^{-14} mol/m^2	Reference permeance coefficient of N_2
$c_{\{H_2,O_2\}}^{ref}$	56.4 and 40 mol/m^3	Reference concentrations of H_2 and O_2
nd	1.1364	Electro-osmotic drag coefficient
$i_{0,ref}^{(an,ca)}$	3×10^4 and 2×10^{-2} A/ m^2	Reference current density at the anode and cathode
Jloss,0	20 A/ m^2	Current density loss constant
Rsolid	0.2×10^{-4} Ω- m^2	Electric resistance of the solid part of the cell
γ_{H_2}	0.5	Concentration coefficient of H_2
γ_{O_2}	1	Concentration coefficient of O_2
$\beta_{\{an,ca\}}$	1 and 1	Transfer coefficients of anode and cathode
$\lambda_{\{an,ca,m\}}$	10	Water content in the anode, cathode, and membrane
$x_{N_2,ca}$	0.78	Molar fraction of nitrogen in the cathode

2.2.1.2. Mass transfer

Maxwell-Stefan equations are utilized to model the species transport through the membrane from and into the anode flow field:

$$\frac{\partial}{\partial t}(\rho w_i) + \nabla \cdot \left(-\rho w_i \sum_j D_{ij} \nabla x_j + \rho w_i U \right) = r_i \tag{6}$$

where w is the mass fraction, x is the mole fraction, ρ is the density, D_{ij} is the binary diffusion coefficient of species i and j, t is time, U is the convective velocity, r is the reaction rate, and ∇ is the differential operator in x and y directions. Species in the anode flow field are hydrogen, H_2, and nitrogen, N_2. Binary diffusion coefficients for species mixtures are given by [67]:

$$D_{ij} = 3.16 \times 10^{-8} \left(\frac{T^{1.75}}{p\left(v_i^3 + v_j^3\right)^2} \right) \left(\frac{1}{M_i} + \frac{1}{M_j} \right)^{1/2} \tag{7}$$

Flow of hydrogen near the inlet is the major part of the convective velocity since a great deal of hydrogen goes into the reaction in the anode catalyst layer and ultra-low stoichiometric flow condition (ULSFC) is applied to the exit flow; thus exit flow is low and its effect on the convective velocity is negligible. Therefore, the convective velocity due to the fluxes of species crossing over the membrane at a certain position is the integral of the sum of the downstream fluxes of species:

$$U_{flux}^{an}(y) = \frac{1}{\rho_{an}} \int_y^L \left(N_{H_2}^{an}(y') + N_{N_2}^{an}(y') \right) dy' \tag{8}$$

Here, L is the length of the channels and N_i^{an} is the inward mass flux of nitrogen from the cathode side and negative of the mass flux of hydrogen that goes to the reaction at the anode catalyst layer.

Flux of nitrogen through the membrane is a function of the difference between the partial pressures of nitrogen in the cathode and anode sides, and calculated as:

$$N_{N_2}^{an} = M_{N_2} \psi_{N_2} \frac{p\left(x_{N_2}^{ca} - x_{N_2}^{an}\right)}{\delta_m} \tag{9}$$

where δ_m is the thickness of the membrane and ψ_{N_2} is the membrane-water-content dependent permeance of nitrogen [21]:

$$\psi_{N_2} = \psi_{N_2}^0 \left(0.0295 + 1.21 f_V - 1.93 f_V^2\right) \exp\left(\frac{E_{N_2}(T - T_0)}{RTT_0}\right) \tag{10}$$

where $\psi_{N_2}^0$ is the reference permeance of nitrogen, E_{N_2} is 24,000 J/mole, and f_V is the volumetric ratio of the liquid water in the membrane and defined as:

$$f_V = \frac{\lambda V_{H_2O}}{V_m + V_{H_2O}} \tag{11}$$

Here, λ is the membrane water content which is equal to the mean of the water content of the anode and cathode (λ_{an}, λ_{ca}), V_m is the molar volume of the dry membrane, and V_{H_2O} is the molar volume of the liquid water in the membrane.

Flux of hydrogen that goes to the reaction is obtained from:

$$N_{H_2}^{an} = -\frac{M_{H_2}}{2F}\left(J_{cell} + J_{loss}\right) \tag{12}$$

where F is the Faraday's constant, J_{cell} is the current density, and J_{loss} is the parasitic current density due to the loss of hydrogen through the anode flow field. Parasitic loss of current is a function of mole fraction of hydrogen:

$$J_{loss} = J_{loss,0} x_{H_2} \tag{13}$$

Here, $J_{loss,0}$ is a constant based on the permeance of hydrogen through the membrane.

The right hand side of the Maxwell-Stefan equation is the reaction rate and it is defined as a function of the mass flux of each species and given by:

$$r_i = \frac{N_i}{d_{eff}} \tag{14}$$

where d_{eff} is the effective depth of the anode channels and it is determined by:

$$d_{eff} = \frac{V_{Total}}{A_{active}} \tag{15}$$

Here, V_{Total} is the total volume available to species, and A_{active} is the active area of the anode channels.

2.2.1.3. Voltage model

Anode is assumed to be the ground electrode and cathode electrode potential is the sum of the reversible cell potential, V_{rev}; ionic potential drop in the membrane, $-\Delta V_m$; the anode activation overpotential, $-\Delta V_{an}$; and the cathode activation overpotential, $-\Delta V_{ca}$; and defined as:

$$V_e = V_{rev} - \Delta V_{an} - \Delta V_{ca} - \Delta V_m \tag{16}$$

The reversible cell potential is:

$$V_{rev} = V_0 + \frac{RT}{2F}\left[\frac{1}{2}\log\left(\frac{c_{O_2}}{c_{O_2}^{ref}}\right) + \log\left(\frac{c_{H_2}}{c_{H_2}^{ref}}\right)\right] \tag{17}$$

where c_i^{ref} is the reference concentration of species i, V_0 is the open-circuit potential which is given by:

$$V_0 = 1.23 - 0.00083 \times (T - 298) \tag{18}$$

Anode and cathode activation potentials are:

$$\Delta V_{an} = \frac{RT}{F\beta_{an}} a\sinh\left[\frac{J_{cell}}{i_{0,ref}^{an}}\left(\frac{c_{H_2}^{ref}}{c_{H_2}^{CL}}\right)^{\gamma_{H_2}}\right] \tag{19}$$

$$\Delta V_{ca} = \frac{RT}{F\beta_{ca}} a\sinh\left[\frac{J_{cell}}{i_{0,ref}^{ca}}\left(\frac{c_{O_2}^{ref}}{c_{O_2}^{CL}}\right)^{\gamma_{O_2}}\left(\frac{c_{H^+}^{ref}}{c_{H^+}^{CL}}\right)^{\gamma_{H^+}}\right] \tag{20}$$

17

Here, β is the transfer coefficient, γ is the concentration coefficient, $i_{0,ref}$ is the reference current density, and c_i^{CL} is the concentration of species i in the catalyst layer, which is calculated from the resistance model in the GDL:

$$c_i^{CL} = c_i - \frac{\delta_{GDL}}{D_{i,N_2}} N_i \tag{21}$$

where δ_{GDL} is the thickness of the GDL, D_{i,N_2} is the binary diffusion coefficient of species i and nitrogen, and N_i is the mass flux of species i.

The ionic potential loss in the membrane is:

$$\Delta V_m = \frac{\delta_m}{\sigma_m} J_{cell} \tag{22}$$

where σ_m is the ionic conductivity of the membrane and defined by an empirical relationship for the Nafion membranes [33]:

$$\sigma_m = \left(-0.326 + 0.514\lambda\right) \exp\left[1268\left(\frac{1}{303} - \frac{1}{T}\right)\right] \tag{23}$$

The cell potential at the cathode electrode is calculated based on the current density and the total electric resistance of the solid components of the cell, R_{solid}, which is estimated from the slope of the polarization curve of the experiments. Cell potential is:

$$V_{cell} = V_e - R_{solid} J_{cell} \tag{24}$$

The integral of the current density, J_{cell}, on the active area of the anode, which includes the anode channels and its feed and exhaust headers, must be equal to the total load current, I_{load}, as follows:

$$\int_{A_{active}} J_{cell} dA = A_{active} J_{load} = I_{load} \tag{25}$$

This study involves anode side analysis and constant values are considered for the cathode side variables. The unknowns are molar fractions of hydrogen and nitrogen, cell

potential, and current density, which are solved by coupling Stokes flow and Maxwell-Stefan models with the developed voltage model.

2.2.2. Numerical Approach

Modeling domain consists of the anode channels and its inlet and outlet configurations. Stokes and Maxwell-Stefan equations, which are subject to a voltage model constraint, are solved in this domain by means of the commercial finite element package, COMSOL Multiphysics [66].

Anode channels' edges are divided into a sufficient number of sections and swept across the channels and GDLs which are between the channels; and triangular mesh with boundary layer are used for the inlet and outlet configurations, as demonstrated in Fig. 2.4. The total number of degrees of freedom is about 3×10^5. Two solvers are used in this study: first, a Fully-coupled solution is used with Newton iterations and direct MUMPS in the stationary solver; then its results are used as the initial condition of the time dependent solver that uses the same Fully-coupled solver with Newton iterations and direct MUMPS.
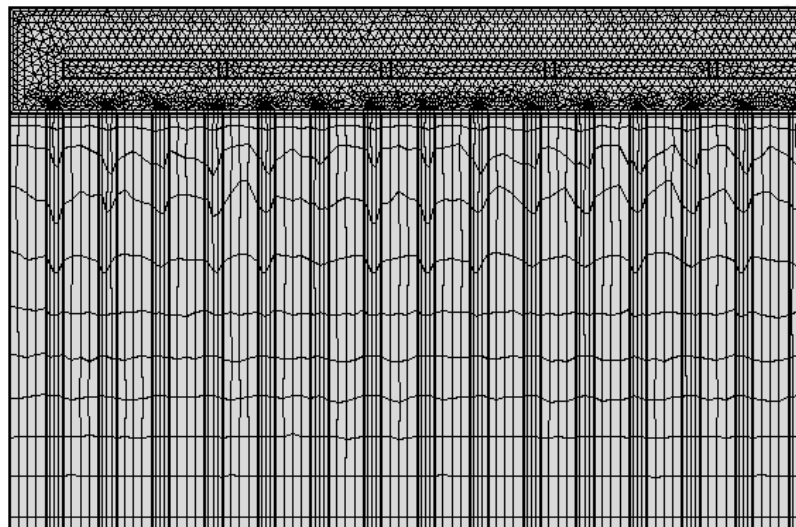
FIGURE 2.4: Distribution of the mesh used for the anode domain.

2.2.3. Performance Metric

The goal of this study is to obtain a uniform distribution of the hydrogen concentration in the anode active area and prevent the blanketing phenomena because of the nitrogen that comes from the cathode side. The final design is a configuration which has a uniform mole fraction of hydrogen close to 1 while hydrogen utilization, which is the ratio of the amount of hydrogen goes to the reaction and hydrogen supplied to the anode inlet, is kept more than 99% (ULS flow condition). For this purpose, the performance metric is defined as the ratio of the area of hydrogen mole fraction less than a certain value, for instance, less than 0.9, to the active area of the anode flow field. This performance metric is called the hydrogen-depletion region ratio and defined as below:

$$\Phi_3 = A\left(x_{H_2} < k\right)\Big/ A_{active} \qquad (26)$$
$$\scriptstyle 0<k<1$$

where $A\left(x_{H_2} < k\right)$ is the area of the domain includes hydrogen mole fraction less than k, the value of k varies between 0 and 1, and A_{active} is the active area.

2.3. Design of Cathode Flow Field

In this section, the goal is to design a flow field for the cathode side of the cell. The model used in this study does not contain species transport through the membrane, and its objective is to find a sufficient amount of pressure drop from the inlet to the outlet.

A three-dimensional model of the cathode flow field consists of parallel serpentine channels, and inlet and outlet manifold is considered, as demonstrated in Fig. 2.5. Serpentine channels are proposed to set an appropriate pressure drop along the channels in order to push out the excess liquid water generated in the cathode active area and membrane, in other words, to prevent the flooding phenomena in the channels. Several separated serpentine channels are used to limit the pressure drop and minimize the parasitic power of the compressor required to pressurize the air supplied to the anode inlet. Using
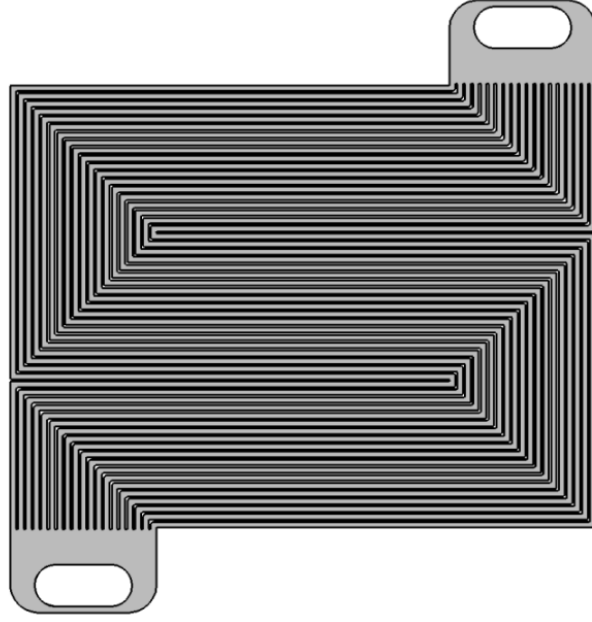
FIGURE 2.5: Geometry of the cathode flow field.

serpentine channels can considerably improve the cell performance at high current operations, as demonstrated in [68].

2.3.1. Governing Equations

In this model, which is the flow analysis in the cathode flow field, Reynolds number is less than 10^3. Therefore, Laminar flow model is used to analyze flow distribution in the cathode flow field. Instead of using pure oxygen, air with high stoichiometry ratio is supplied to the cathode flow field.

Laminar flow equations are:

$$-\nabla p + \mu \nabla^2 \mathbf{u} = \rho (\mathbf{u}.\nabla) \mathbf{u} \qquad (27)$$

where p is the pressure, $\mathbf{u}$ is the velocity vector, ρ is the density of the fluid, and μ is the dynamic viscosity of the fluid. Moreover, air is an incompressible fluid and it is subjected to the continuity equation:

$$\nabla.\mathbf{u} = 0 \qquad (28)$$
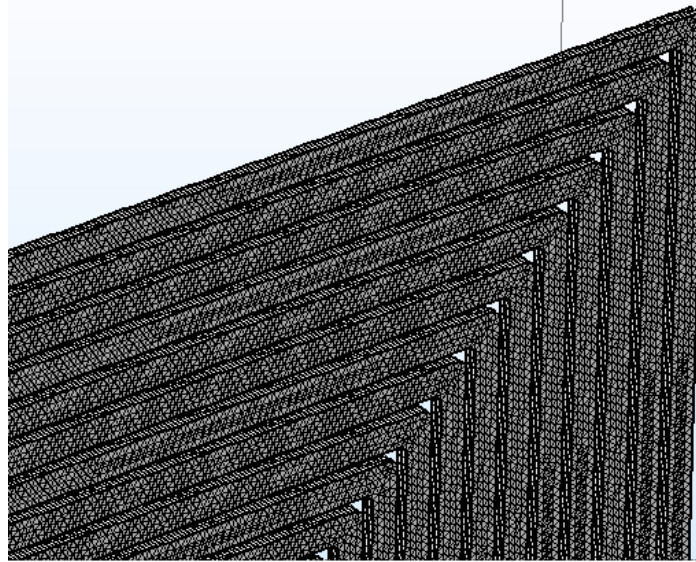
FIGURE 2.6: Mesh distribution in the cathode flow field.

Boundary conditions are determined as a constant mass flow rate and a constant pressure for the inlet and outlet manifolds, respectively. Inlet mass flow rate is set to 2.687×10^{-4} kg/s and the outlet pressure is set to 1.5 atm.

2.3.2. Numerical Approach

In this study, modeling domain is the cathode channels and its inlet and outlet configurations. Laminar flow equations are applied to this domain by means of the commercial finite element package, COMSOL Multiphysics [66].

A triangular mesh is used for the top surface of the cathode flow field and swept across the depth of the field to obtain prismatic elements, as demonstrated in Fig. 2.6. The total number of degrees of freedom is about 3×10^{6}. The fully-coupled solution is used with Newton iterations and direct PARDISO solver.

2.4. Design of Cooling Flow Field

In this section, the goal is to design an effective flow field for the cooling side of the cell. The objective of this study is to find a uniform temperature distribution in the cell with a very low temperature variation to avoid degradation in the membrane and catalyst layers.

Several cooling methods exist: (1) using materials with high thermal conductivity or heat pipes, which is called cooling with the heat spreaders; (2) using a separated air flow field; (3) supplying more air to the cathode flow field; (4) using a liquid flow field; (5) phase change cooling. The first and two last methods are not affordable in the automotive (high power) PEMFC stacks. For the same parasitic power used in the pump or compressor, heat transfer coefficients with liquid like water are much higher than that with air flow [69].

The most common technique that has been used in the high power PEM fuel cells is water cooling. Since the goal is to design a PEMFC stack for an automotive application with the power output about 50 kW, water flow field is utilized between the cells. Serpentine channels flow field, like the configuration used for the cathode flow field, is used for the cooling flow field. This configuration consists of serpentine channels, and inlet and outlet manifolds, as demonstrated in Fig. 2.7.
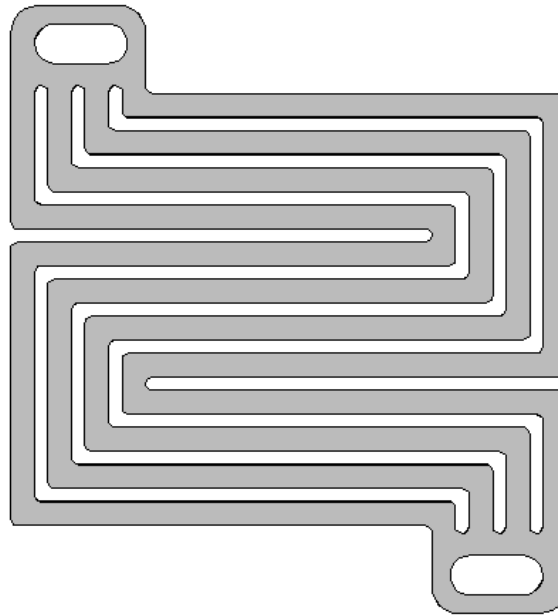
FIGURE 2.7: Geometry of the cooling flow field.

2.4.1. Governing Equations

Laminar flow equations are used to analyze the flow distribution in the cooling flow field. In addition, conjugated heat transfer equations are utilized to investigate the temperature distribution through the cooling plate.

2.4.1.1. Laminar flow

Laminar flow analysis is used in this model, which is flow analysis in the cooling flow field, since Reynolds number is less than 10. The analysis and equations used for the Laminar flow model in the cooling flow field are similar to the ones used in the cathode flow field (section 2.3.1). The only difference is the inlet boundary condition, which is pressure in this model. Constant pressure boundary conditions are used at the inlet and outlet manifolds to obtain a fixed pressure difference between them (2 kPa).

2.4.1.2. Heat transfer

Conjugate heat transfer analysis corresponds to the combination of heat transfer in the solids and fluids, which are graphite and water respectively in this study, is used. Heat transfer equation used in this model is:

$$\rho C_p \mathbf{u}.\nabla T + \nabla.\mathbf{q} = Q \tag{29}$$

where ρ is the density of the fluid, C_p is the heat capacity of the fluid at constant pressure, $\mathbf{u}$ is the velocity vector, T is the temperature vector, $\mathbf{q}$ is the heat flux vector, and Q is the heat. The first term in the above equation is related to the convective heat transfer in the fluid and the second term is related to the conductive heat transfer in the solid. Heat flux is defined as:

$$\mathbf{q} = -k\nabla T \tag{30}$$

where k is the thermal conductivity of the solid used in the model.

Constant temperature is specified at the inlet manifold and a heat flux is applied to the top surface of the cathode active area. Inlet temperature is set to 80 °C, which is the operation temperature of the cell; and the heat flux is set to 6×10^3 W/m^2, which is equal to the electrical power of the cell and it is one of the design assumptions.

2.4.2. Numerical Approach

In this study, modeling domain consists of cooling channels and their inlet and outlet manifolds. Laminar flow and heat transfer equations are applied to this domain by means of the commercial finite element package, COMSOL Multiphysics [66].

A triangular mesh is used for the top surface of the cooling flow field and swept across the depth of the flow field to obtain prismatic elements, as demonstrated in Fig. 2.8. The total number of degrees of freedom is about 2×10^5. The segregated solution is used with Newton iterations and direct PARDISO solver.
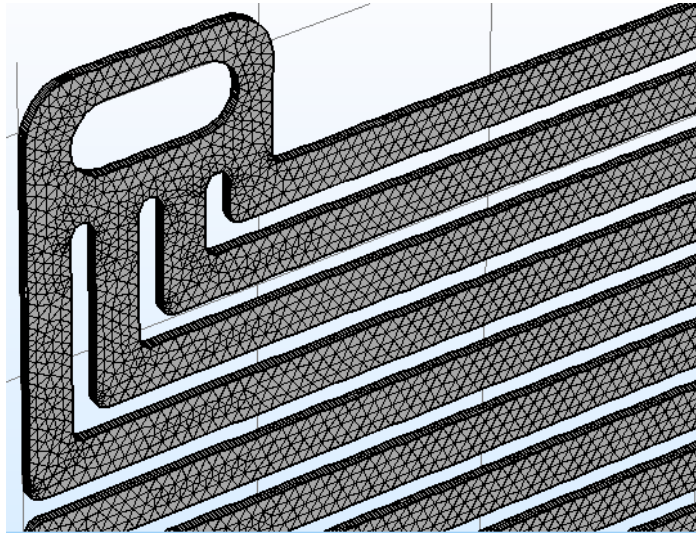
FIGURE 2.8: Mesh distribution in the cooling flow field.

2.5. Model of Liquid Water Transport and Distribution through Channels and GDLs

In this section, the goal is to introduce a complete model which contains the anode and cathode channels and GDLs. Further, this model is the most accurate model since it contains both species and liquid water transport in the cell. Because of the complexity of this model, it is one-dimensional. Moreover, the result of this model is compared with the experimental data provided by [65].

A one-dimensional model of the anode channel, anode GDL, cathode channel, and cathode GDL is developed. This model is the improved form of the model used to investigate the nitrogen accumulation in the anode flow field (section 2.2), since: (1) cathode flow field is included in the Maxwell-Stefan model; (2) water vapor mole fraction is included in the Maxwell-Stefan model; (3) condensation and evaporation of the water generated in the cell is considered; (4) transport and distribution of the liquid water through the anode and cathode channels and their GDLs are considered in this model. Including liquid water distribution and transport in this model makes its results more realistic and practical than the models neglect the liquid water in the cell and assume the instant evaporation of the liquid water in the cell components.

2.5.1. Governing Equations

Maxwell-Stefan equations are solved to investigate the transport and distribution of the species through the anode and cathode channels and their GDLs due to the convection and diffusion of the species. A voltage model is used to investigate the current density distribution and hydrogen consumption rate (reactions kinetics), and this model will be coupled to the Maxwell-Stefan equations. Lastly, a liquid water model is used to simulate the liquid water transport and distribution through the anode and cathode channels and their GDLs.

2.5.1.1. Mass transfer

Maxwell-Stefan equations are utilized to analysis the transient transport and distribution of the species through the anode and cathode channels and their GDLs:

$$\frac{\partial}{\partial t}(\rho w_i) + \frac{\partial}{\partial z}\left(-\rho w_i \sum_j D_{ij} \frac{\partial x_j}{\partial z} + \rho w_i U\right) = r_i \tag{31}$$

where x is the mole fraction, w is the mass fraction, ρ is the density of the mixture, D_{ij} is the coefficient of the binary diffusion of species i and j, z is the axis coordinate in the direction of the flow in the anode and cathode channels, r is reaction rate, and U is the convective velocity in the anode and cathode channels. Species in the anode side analysis are hydrogen (H_2) that is supplied to the anode inlet, nitrogen (N_2) that comes from the cathode side, and water vapor (H_2O). Species in the cathode side analysis are oxygen (O_2) and nitrogen (N_2) which come from the air supplied to the cathode inlet, and water vapor (H_2O). Mole or mass fraction of two species at each side is solved and the last one is determined by the conservation of mass:

$$\sum x_i = 1 \tag{32}$$

Binary diffusion coefficient of species in a mixture is defined as [67]:

$$D_{ij} = 3.16 \times 10^{-8} \left(\frac{T^{1.75}}{p\left(v_i^3 + v_j^3\right)^2}\right)\left(\frac{1}{M_i} + \frac{1}{M_j}\right)^{1/2} \tag{33}$$

where T is the operation temperature, p is the operation pressure, and v_i and M_i are the molar volume and molecular weight of species i, respectively. Dalton's Law is used to determine the density of the mixture in the anode and cathode channels:

$$\frac{1}{\rho} = \frac{\sum_i \dfrac{w_i}{M_i}}{\dfrac{p}{RT}} \tag{34}$$

Convective velocity is determined by the summation of the exit flow velocity and the flux of the species reacting at the catalyst layer and exchange through the membrane:

$$U = U_{exit} + U_{flux} \tag{35}$$

In the anode side, the flow of hydrogen at the inlet is the major part of the convective velocity of the anode channel. Exit flow velocity in the anode side is 0 since dead-ended condition is applied to the anode exit and all hydrogen supplied to the anode channels is expected to enter the reaction at the anode catalyst layer. Thus, the convective velocity in the anode channel due to the flux of the species crossing over the membrane at a certain position is the integral of the sum of the downstream fluxes of species:

$$U_{flux}^{an}(z) = \frac{1}{\rho_{an}} \int_z^L \left(N_{H_2}^{an}(z') + N_{N_2}^{an}(z') + N_{H_2O}^{an}(z') \right) dz' \tag{36}$$

where L is the length of the anode channel, $N_{N_2}^{an}$ and $N_{H_2O}^{an}$ are inward fluxes of nitrogen and water vapor come from the cathode side, and $N_{H_2}^{an}$ is outward flux of hydrogen that goes into the reaction at the anode catalyst layer and defined as:

$$N_{H_2}^{an} = -\frac{M_{H_2}}{2F} \left(J_{cell} + J_{loss} \right) \tag{37}$$

where F is Faraday's constant, J_{cell} is the current density, and J_{loss} is the parasitic current density due to the loss of hydrogen that enters the reaction and defined as a function of mole fraction of hydrogen:

$$J_{loss} = J_{loss,0} x_{H_2} \tag{38}$$

Here, $J_{loss,0}$ is a constant determined from the permeance of hydrogen through the membrane.

Inward flux of nitrogen which comes to the anode side is a function of the difference between the partial pressure of nitrogen in the cathode and anode channels:

$$N_{N_2}^{an} = M_{N_2} \psi_{N_2} \frac{p \left(x_{N_2}^{ca} - x_{N_2}^{an} \right)}{\delta_m} \tag{39}$$

where δ_m is the thickness of the membrane, and ψ_{N_2} is the membrane-water-content dependent coefficient of the nitrogen permeance through the membrane and defined by [21]:

$$\psi_{N_2} = \psi_{N_2}^0 \left(0.0295 + 1.21 f_V - 1.93 f_V^2 \right) \exp\left(\frac{E_{N_2}(T - T_0)}{RTT_0} \right) \tag{40}$$

Here, $\psi_{N_2}^0$ is the reference coefficient of nitrogen permeance, E_{N_2} is 24,000 J/mole, and f_v is the volumetric ratio of the liquid water in the membrane and determined by:

$$f_V = \frac{\lambda V_{H_2O}}{V_m + V_{H_2O}} \tag{41}$$

where λ is the membrane water content and defined as the molar ratio of water molecules per sulfonic group in the membrane, V_{H_2O} and V_m are molar volumes of the liquid water and dry membrane, respectively. Membrane water content is the mean of the water content of the anode and cathode sides:

$$\lambda = \frac{\lambda_{an} + \lambda_{ca}}{2} \tag{42}$$

The water content of the anode and cathode sides are functions of the water activity of each side and the operation temperature, and it is interpolated from the experimental data at $T = 30$ and 80 °C. Water activity is determined by:

$$a = x_{H_2O} \frac{P}{P_{sat}(T)} \tag{43}$$

where $P_{sat}(T)$ is the saturated pressure of water at the operation temperature.

Inward flux of the water vapor which comes to the anode side is a function of the membrane water content at the anode and cathode sides, and current density, and it is given by:

$$N_{H_2O}^{an} = M_{H_2O} \left[\frac{c_{SO_3}^0 \left(\lambda_{ca} - \lambda_{an} \right)}{R_m} - n_d \frac{J_{cell}}{F} \right] \tag{44}$$

Here, $c_{SO_3}^0$ is the concentration of sulfonic in the dry membrane, n_d is the electro-osmotic drag coefficient, and R_m is the resistance to the water transport across the membrane and determined by:

$$R_m = \frac{1}{k_{ads}} + \frac{1}{k_{des}} + \frac{\delta_m}{D_\lambda} \tag{45}$$

where k_{ads} and k_{des} are the adsorption and desorption coefficients, and D_λ is the diffusion coefficient of water in the membrane; these coefficients are given by [70]:

$$k_{ads} = 1.14 \times 10^{-5} f_v \exp\left[2416 \left(\frac{1}{T} - \frac{1}{T_0} \right) \right] \tag{46}$$

$$k_{des} = 4.59 \times 10^{-5} f_v \exp\left[2416 \left(\frac{1}{T} - \frac{1}{T_0} \right) \right] \tag{47}$$

$$D_\lambda = 2.72 \times 10^{-9} f_\lambda \exp\left[2416 \left(\frac{1}{T} - \frac{1}{T_0} \right) \right] \tag{48}$$

In the cathode side, the convective velocity is determined by the exit flow velocity plus the flux of the species reacting at the catalyst layer and exchange through the membrane, like the anode side. Velocity due to the flux of the species at a certain position is the integral of the sum of the downstream fluxes of species and it is determined as:

$$U_{flux}^{ca}(z) = \frac{1}{\rho_{ca}} \int_z^L \left(N_{O_2}^{ca}(z') + N_{N_2}^{ca}(z') + N_{H_2O}^{ca}(z') \right) dz' \tag{49}$$

The flux of oxygen that goes to the reaction at the cathode catalyst layer is given by:

$$N_{O_2}^{ca} = -\frac{M_{O_2}}{4F} \left(J_{cell} + J_{loss} \right) \tag{50}$$

The flux of water vapor in the cathode side is:

$$N_{H_2O}^{ca} = M_{H_2O} \left[-\frac{c_{SO_3}^0 \left(\lambda_{ca} - \lambda_{an} \right)}{R_m} + \left(n_d + 0.5 \right) \frac{J_{cell}}{F} \right] \tag{51}$$

The flux of nitrogen in the cathode side is the negative of the inward flux of nitrogen that goes to the anode side.

The right hand side of the Maxwell-Stefan equation is the reaction rate and it is defined as a function of the mass flux of each species and given by:

$$r_i = \frac{N_i}{d_{eff}} \tag{52}$$

where d_{eff} is the effective depth of the anode and cathode channels and it is determined by:

$$d_{eff} = \frac{V_{Total}}{A_{active}} \tag{53}$$

Here, V_{Total} is the total volume available to the species, and A_{active} is the active area of the anode and cathode channels.

2.5.1.2. Voltage model

Analysis and equations used in this voltage model are similar to the ones used in the voltage model of the two-dimensional model of the anode flow field (section 2.2.1.3).

2.5.1.3. Liquid water model

In this section, evaporation and condensation of the water exists in the anode and cathode channels and their GDLs, and transportation of the liquid water between the channels and GDLs and between the GDLs are investigated. The membrane and anode and cathode catalyst layers are neglected in this model. Values of the constants used in this model are listed in table 2.2.

Table 2.2: Constants of liquid water model

Parameter	Value	Description
K_{cond}	6.5×10^{-4}	Condensation coefficient
K_{evap}	5.5×10^{-6}	Evaporation coefficient
K_m	1.0×10^{-10} m^2	Membrane permeability
$K_0^{\,l}$	3×10^{-12} m^2	Intrinsic permeability of the GDL
δ_{gdl}	300×10^{-6} m	Thickness of the GDL
ε	0.6	Porosity of the GDL

For the phase change of water between the vapor and liquid phases, the following equation is used [71]:

$$S_{H_2O}^{phase} = \begin{cases} K_{cond}\Delta P \dfrac{\varepsilon(1-S)x_{H_2O}M_{H_2O}}{RT}, \Delta P \geq 0 \\ K_{evap}\Delta P \varepsilon S \rho, \Delta P < 0 \end{cases} \tag{54}$$

where K_{cond} is the condensation coefficient, K_{evap} is the evaporation coefficient, ε is the porosity of the GDL (this parameter is fixed to 1 for applying this equation to the channels), S is the liquid water saturation, and ΔP is the pressure difference from the saturation pressure of water and defined as:

$$\Delta P = P x_{H_2O} - P_{sat} \tag{55}$$

For the transport of the liquid water between channels and their GDLs and between GDLs, the following equation is considered:

$$\frac{\partial S}{\partial t} + \nabla.\left(-D_s \nabla S + S\mathbf{u}\right) = R \tag{56}$$

where S is the liquid water saturation, D_s is the diffusion coefficient, $\mathbf{u}$ is the velocity field, and R is the reaction rate. Diffusion coefficient, which is often called the capillary diffusivity, is determined as:

$$D_s = \frac{K^l}{\mu_l}\frac{dP_c}{dS} \tag{57}$$

32

Here, K^l is the liquid-phase permeability and P_c is the capillary pressure, these two parameters are functions of liquid water saturation. The capillary pressure is the difference between the pressure of the liquid and gas water phases, $P_c = P_g - P_l$. For the channels, the capillary diffusivity (D_s) is kept constant [71], however, dP_c/dS is kept constant for the GDLs [72-73]. The liquid-phase permeability of the GDLs is determined by:

$$K^l = K_0^l S^4 \tag{58}$$

where K_0^l is the intrinsic permeability of the GDLs.

The reaction rate (R) is defined linearly as a function of the difference between the liquid water saturation of the channels and their corresponding GDLs, for instance, the reaction rate of the liquid water from the anode GDL to the anode channel is determined as:

$$R_{an} = C\left(S_{angdl} - S_{anch}\right) \tag{59}$$

Here, C is a constant, S_{anch} and S_{angdl} are the liquid water saturation in the anode channel and GDL, respectively.

The reaction rate between the anode and cathode GDLs is determined by:

$$R_{gdl} = \frac{K_m\left(P_l^{ca} - P_l^{an}\right)}{\delta_{gdl}\varepsilon\rho} \tag{60}$$

where K_m is the membrane permeability, δ_{gdl} is the thickness of the GDL, and P_l^{ca} and P_l^{an} are the pressure of the liquid water in the cathode and anode GDLs, respectively. These liquid water pressures are functions of the liquid water saturation, and they are determined by an interpolation applied to the experimental data provided by [63].

The unknowns of this study are: molar fractions of hydrogen, nitrogen, and water vapor in the anode flow field, x_i^{an}; molar fractions of oxygen, nitrogen, and water vapor in the cathode flow field, x_i^{ca}; current density, J_{cell}, and cell potential, V_{cell}; and liquid water saturations in the anode and cathode channels and their GDLs, S_i. These 12 unknowns are obtained by solving the Maxwell-Stefan equations coupled with the voltage and liquid water models.

3. RESULTS AND DISCUSSION

3.1. Results of Optimization of Flow Velocity Distribution through Anode Channels by Neglecting Species Transport

Searching for a uniform flow distribution in the anode channels consists of four steps. The first is a search among general models with different position of inlet and outlet manifolds, and adjusting their best case to be used in the cell structure. In the second step, effects of the channels and ribs widths are studied for the best case of the previous step. Thirdly, inlet configuration of the model is studied for different size and position of the inlet baffle(s) in the feed header. Finally, the position and size of the outlet baffle(s) are studied for different inlet configurations.

Structured optimization algorithm such as genetic algorithm is not applicable to this analysis since a wide range of the variables is considered for the position, size, and number of the inlet and outlet baffles. Hence, an unstructured search is used for each part of the model, and for fixed topologies a simple grid-type search is utilized over their variables. Final design is quantified by less than 5% rms value among the channels velocities, and maximum to minimum channel-velocity ratio less than 1.2, which indicates that maximum velocity has to be less than 20% greater than minimum velocity in the channels.

3.1.1. Effects of Inlet and Outlet Manifolds

First, the flow distributions of five models with different inlet and outlet configurations are analyzed, as represented in Fig. 3.1. In all cases feed header (FH) is placed at the top and exhaust header (EH) is located at the bottom of the parallel (main)
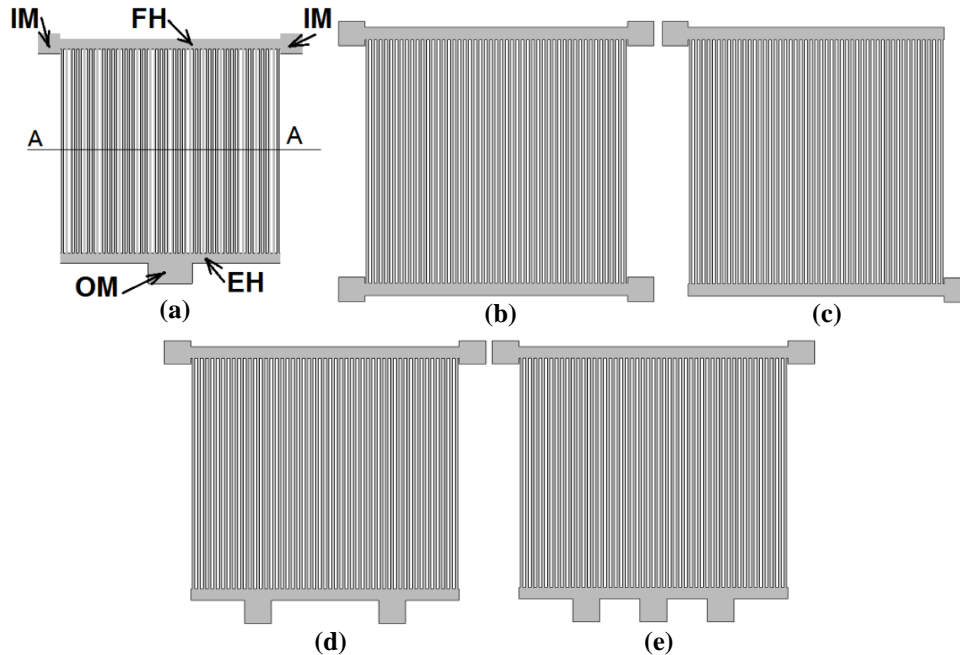
FIGURE 3.1: Inlet and exhaust manifold configurations; flow enters at the top and exits at the bottom. In a, IM stands for Inlet manifold, OM for outlet manifold, FH for feed header, and EH for exhaust header; section A-A shows where the channel velocities are obtained.

channels. Widths of the channels used for the FH and EH are greater than the widths of the main channels. By means of an inlet or inlets on the FH, flow is supplied to the channels. Then, flow is gathered up from the channels and pushed out across an outlet or outlets on the EH. All cases, except case c which has one inlet manifold, have two inlet manifolds on the sides of the feed header. Case a has a single outlet manifold placed at the middle of the exhaust header and other cases have multiple outlet manifolds located on the exhaust header. In this analysis, the channels and ribs widths are considered constant and equal.

The configuration demonstrated in Fig. 3.1a contains of two inlet manifolds (IMs) at the edges of the feed header (FH) and an outlet manifold (OM) at the middle of the exhaust header (EH). In this model, the length of the OM is twice the IM and they have the same widths. This design is promising since the IMs supply flow to the channels close to the edges and the OM at the middle of the EH collects flow from the center, which will result in uniformity of the flow distribution and reduce pressure differences between channels. Figure 3.1b represents a configuration has two IMs at the edges of the FH and two OMs
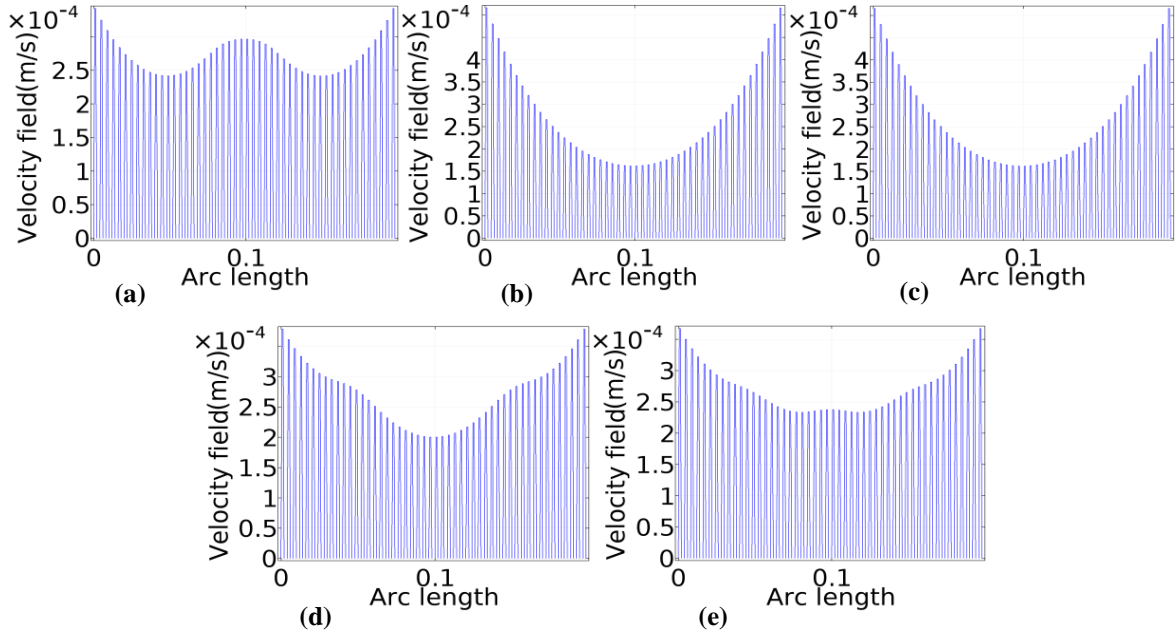
FIGURE 3.2: Flow distribution in the channels for the inlet and outlet manifolds structures given in Fig. 3.1, respectively.

at the edges of the EH. Figure 3.1c indicates a configuration has an IM at the left edge of the FH and an OM at the right edge of the EH. Figure 3.1d illustrates a configuration which contains two IMs at the edges of the FH and two OMs off-center half-way between the edges and the center of the EH. The last configuration has one more OM in the middle of the EH in addition to the previous configuration, as shown in Fig. 3.1e.

Velocity distributions of the configurations stated in Fig. 3.1 are demonstrated in Fig. 3.2, respectively. Velocities are obtained in the center of the length and depth of the anode channels (section A-A in Fig. 3.1a). In all designs, there are two maximum velocities at the sides (edges) channels where are below the inlet(s) and over outlet(s). In case a, there is another maximum velocity in the central channels where the flows, which come from the IMs at the sides of the FH, intersects with each other and it is above the OM. Configurations of Figs. 3.2b and 3.2c have maximum velocities, near the edges of the plate, which are more than twice higher than the minimum velocity in the middle channels. For all configurations in Fig. 3.2a to 3.2e; Φ_1 values are 1.4162, 3.1855, 3.18118, 1.8902, and 1.5745; and Φ_2 values are 0.09922, 0.3906, 0.3904, 0.1900, and 0.2198, respectively. Therefore, the optimum design, which has the minimum values of the performance metrics,
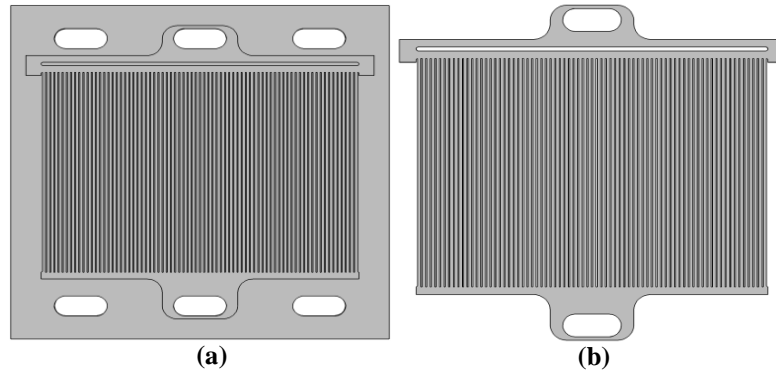
FIGURE 3.3: (a) Anode side of the cell showing all the ports; (b) anode flow field with a baffle at the feed header.

is obtained for configuration in Fig. 3.1a where IMs are at the edges of the FH and OM is at the middle of the EH.

This optimum design cannot be implemented to the anode side of the cell because of the multiplicity of the inlet manifolds. There are three holes in the top and three holes in the bottom of the final design of the cell configuration for the anode side, cathode side, and cooling side, as demonstrated in Fig. 3.3a. Only one of the inlet and outlet holes among these three inlet and outlet holes can be used for the anode side. The configuration that gives the similar performance as optimum case (Fig. 3.1a) contains an IM in the middle of the FH, an OM in the middle of the EH, and a barrier under the IM and over the main channels, as illustrated in Fig. 3.3b.

3.1.2. Effects of Channel and Rib Widths

The modified configuration in Fig. 3.3b is investigated for different channel and rib widths. First, the rib width is set to 2 mm and the channel width varies from 2 to 5 mm. Then, the channel width is set to 2 mm and the rib width varies from 0.75 to 2 mm.

In Fig. 3.4a, Φ_1 and Φ_2 are indicated as a function of the channels width when the width of the ribs is kept constant as 2 mm. The maximum value of the maximum to minimum channel-velocity ratio, Φ_1, is for the channel width equal to 3 mm. The rms value of the channel velocities increases relatively sharply from 0.23 to 0.25 between 2 and 3 mm
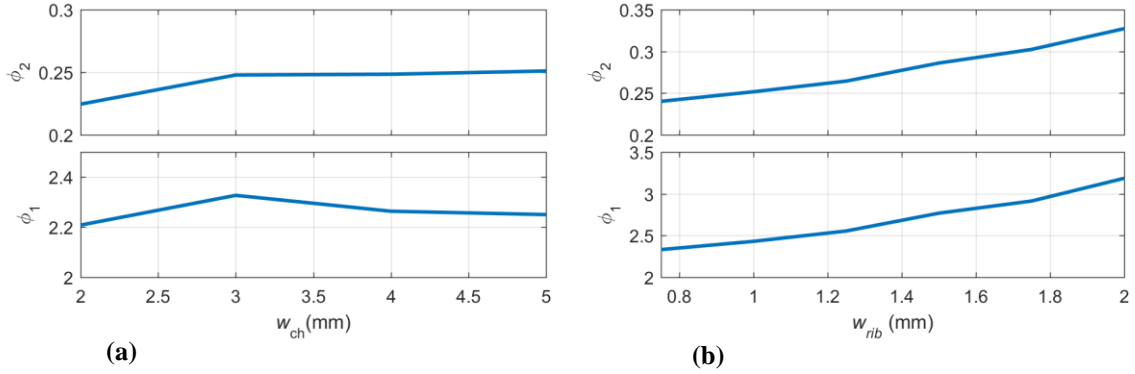
37

FIGURE 3.4: Φ_1 and Φ_2 vs w_{ch} when $w_{rib}=2$ mm (a); and Φ_1 and Φ_2 vs w_{rib} when $w_{ch}=2$ mm (b).

widths, then remains almost constant around 0.25. The lowest values of Φ_1 and Φ_2 are obtained for the smallest channel width, $w_{ch}=2$ mm, as demonstrated in Fig. 3.4a. Smaller channels widths are not analyzed to avoid long channels with small cross-sections, which may have adverse effects for the DEA or ULS operation of the fuel cell as discussed by McKahn [74]. Nevertheless, the variation of the performance metrics with the channel width remains very small for the lower channel widths.

Figure 3.4b represented the variation of Φ_1 and Φ_2 with the width of the ribs. Both metrics increase with the increase in the width of the ribs. The lowest values of Φ_1 and Φ_2 are obtained for ribs with 0.75 mm width. Further decrease in the width of the ribs is not investigated since they are not practical due to the mechanical and electrical concerns as ribs deform the gas diffusion layer and a further decrease in the contact area may increase the electrical resistance and the associated potential drop.
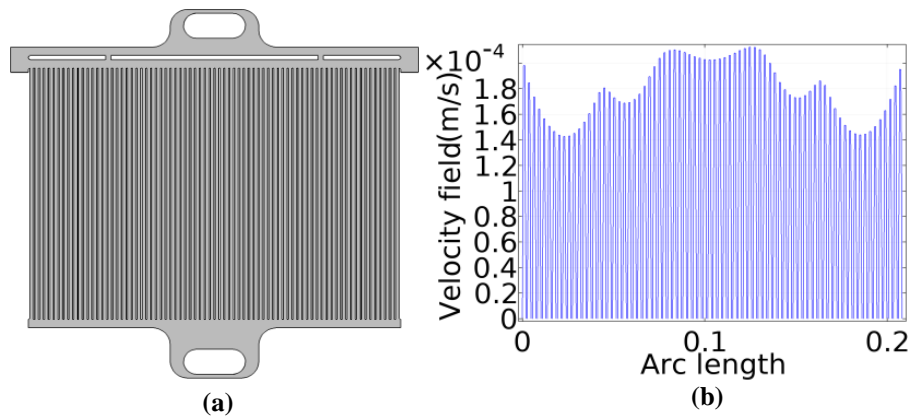

FIGURE 3.5: (a) Three-segmented FH baffle configuration; (b) velocity distribution in the channels for $d_1=6$cm and $w_{gap1}=1$mm.
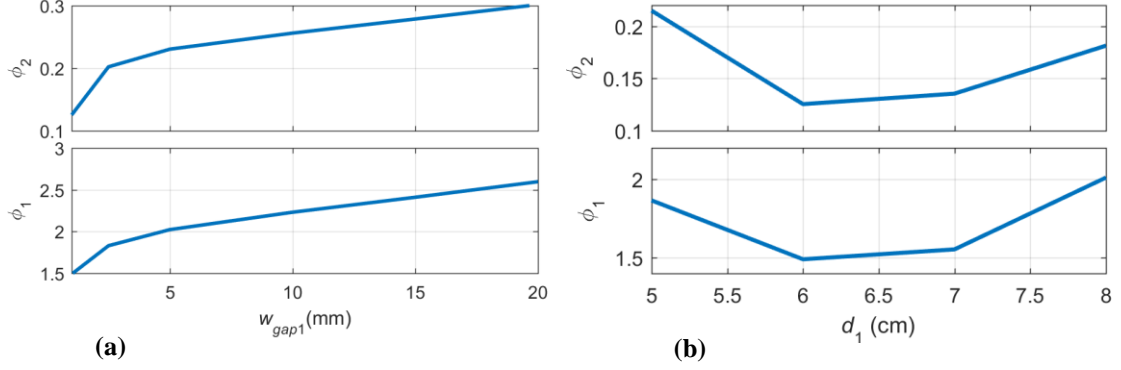
38

FIGURE 3.6: Effects of the length of the central segment and gap width for 3-segmented FH baffle: (a) Φ_1 and Φ_2 vs w_{gap1} for d_1=6cm, (b) Φ_1 and Φ_2 vs d_1 for w_{gap1}=1mm.

3.1.3. Design of Feed Header

In order to improve the velocity distribution, the baffle inside the feed header (FH) is divided into three segments. One large segment where is in the middle and two smaller and symmetric segments near the sides, as demonstrated in Fig. 3.5a. The length of the central segment is specified as $2d_1$, and varies between 10 and 16 cm, the width of the gaps between the segments are specified as w_{gap1} and varies between 1 and 20 mm. The total length of the three segment baffles including the gaps width between them remains constant and the same as the baffle size used in Fig. 3.3b, i.e. 20 cm.

The variation of Φ_1 and Φ_2 with respect to d_1 and w_{gap1} are investigated, respectively, as indicated in Figs. 3.6a and 3.6b. In the search with respect to d_1 the gap width, w_{gap1}, is kept constant as 1 mm, and in the search with respect to w_{gap1}, d_1 is set to 6 cm. As the widths of the gaps increases, Φ_1 and Φ_2 increase with a sharp change between 1 and 2mm, as shown in Fig. 3.6a. On the other hand, Φ_1 and Φ_2 go through a minimum around d_1= 6 cm and then increase gradually, as illustrated in Fig. 3.6b. The best case is obtained for d_1=6 cm and w_{gap1}=1 mm, and its performance metrics values are 1.49 and 0.1255 for Φ_1 and Φ_2, respectively. Since the values of Φ_1 and Φ_2 are worse than the case shown in Fig. 3.1a, alternative designs are necessary.

In order to improve the previous design, the length of the side segments, d_2, is varied from 1.5 to 4 cm, which causes vary in the total length of the inlet baffle. Furthermore, this analysis is applied to the optimal case of the previous design, i.e. d_1=6 cm and w_{gap1}=1 mm.
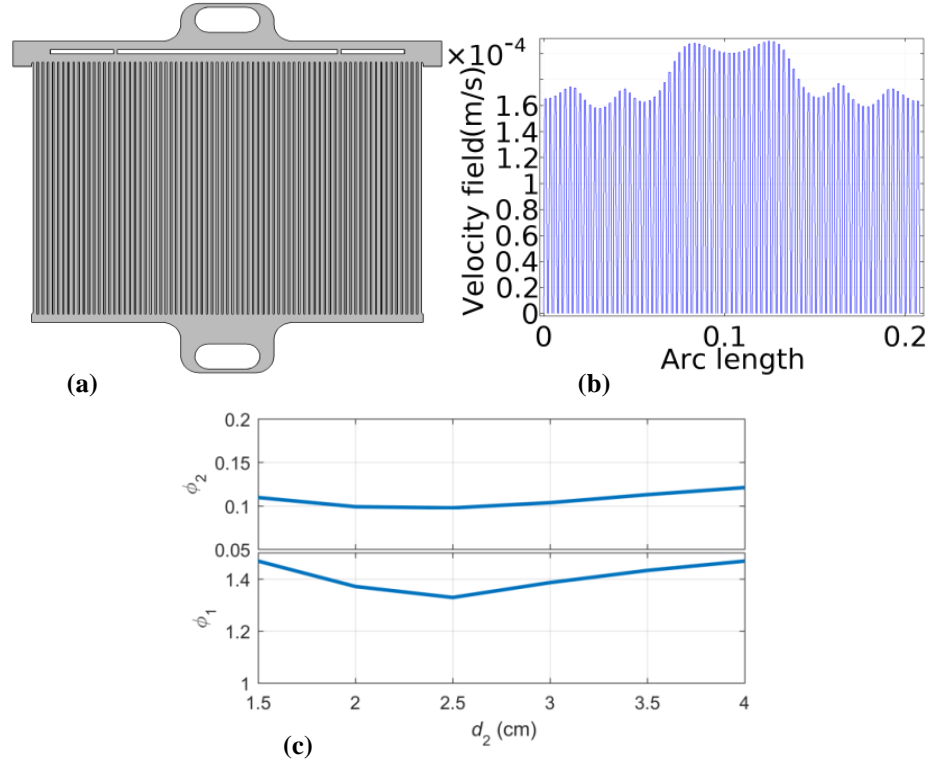
(a)

(b)

(c)

FIGURE 3.7: (a) Segmented FH baffle configuration with 2.5 cm side segments; (b) Channel velocity distribution for w_{gap1}=1mm, d_1=6cm, and d_2=2.5cm; (c) Φ_1 and Φ_2 vs d_2 for w_{gap1}=1mm and d_1=6cm.

This configuration is illustrated in Fig. 3.7a for d_2=2.5 cm. Figure 3.7c shows the variation of the performance metrics as a function of d_2. The best case of this design is for d_2=2.5 cm and its corresponding values of Φ_1 and Φ_2 are 1.328 and 0.0976, respectively, which are significantly lower than the ones obtained for the fixed side segments with d_2=4 cm. Figure 3.7b demonstrates the flow distribution in the channels at the section A-A for the optimum case of this configuration.

The last step in improving the FH design is considering five segments in the inlet baffle while its length is kept constant at 20 cm, as demonstrated in Fig. 3.8a. The length of the central segment is $2d_1$, the length of the inner side segments is d_2, and the width of the gaps between the segments is set to 1 mm. The length of the outer side segments can be obtained from the overall length of the inlet baffle, the lengths of the inner segments, and the width of the gaps between them. Figure 3.8b illustrates the velocity distribution in the channels of this configuration for $2d_1$=13 cm and d_2=1 cm.
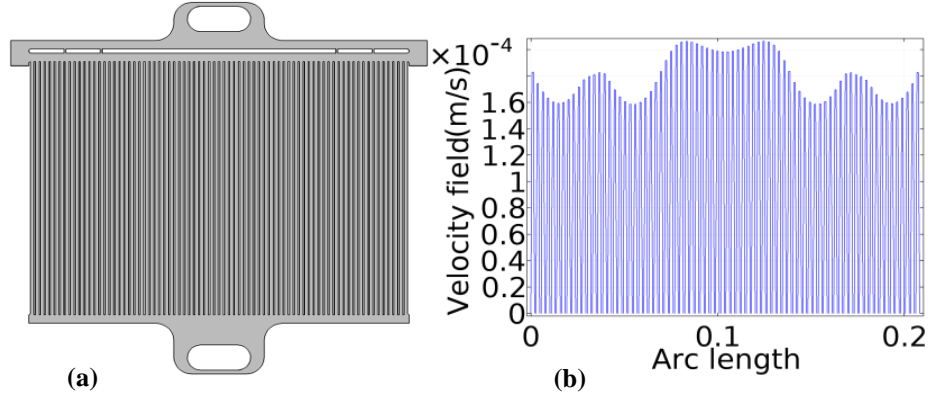
40

(a)   **(b)**

FIGURE 3.8: (a) Inlet configuration with a 5-segment baffle; (b) Flow distribution for w_{gap1}=1mm, d_1=6.5cm and d_2=1cm.

Figures 3.9a and 3.9b demonstrate the variation of Φ_1 and Φ_2 with respect to d_1 and d_2, respectively. Slight but further improvement in the uniformity of the flow in the channels is obtained: best values of Φ_1 and Φ_2 are obtained as 1.3018 and 0.0848 for $2d_1$=13 cm and d_2=1 cm.

Further segments in the FH baffle are not studied as the improvement is very small in channel-velocity distribution quantified by the performance metrics. Moreover, based on the observation of large velocities in the central channels and in order to see the effect of the exhaust header (EH) on the channel- velocity distribution, effects of the EH topology are studied next.

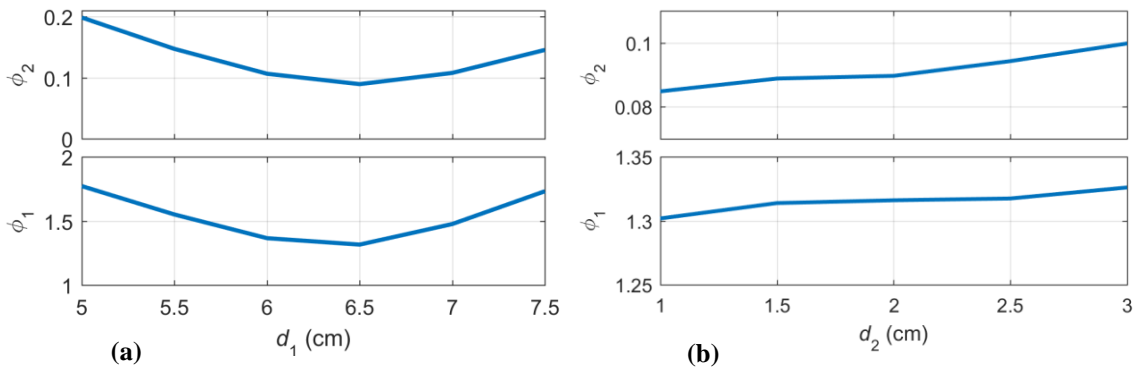**(a)**   **(b)**

FIGURE 3.9: (a) Φ_1 and Φ_2 vs d_1 for w_{gap1}=1mm and d_2=2cm; (b) Φ_1 and Φ_2 vs d_2 for w_{gap1}=1mm and d_1=6.5cm.

41

3.1.4. Design of Exhaust Header

Two baffles are introduced in the exhaust header, as indicated in Fig. 3.10a. This configuration is the main or the best idea for the exhaust header design since the most problematic issue in the flow distribution of different inlet configurations is a maximum velocity in the central channels. Indeed, this maximum velocity is caused by the position of the outlet manifold where is below the central channels and accordingly it supplies more flow to these channels. By means of these outlet baffles where are above the outlet manifold, more flow passes through the channels in the middle of each side and near the edges. Along with the geometry of the exhaust baffles; the geometry of the three-segmented inlet baffle is also varied to obtain a more suitable flow distribution here. Figure 3.10b shows the final flow distribution for the configuration illustrated in Fig. 3.10a.

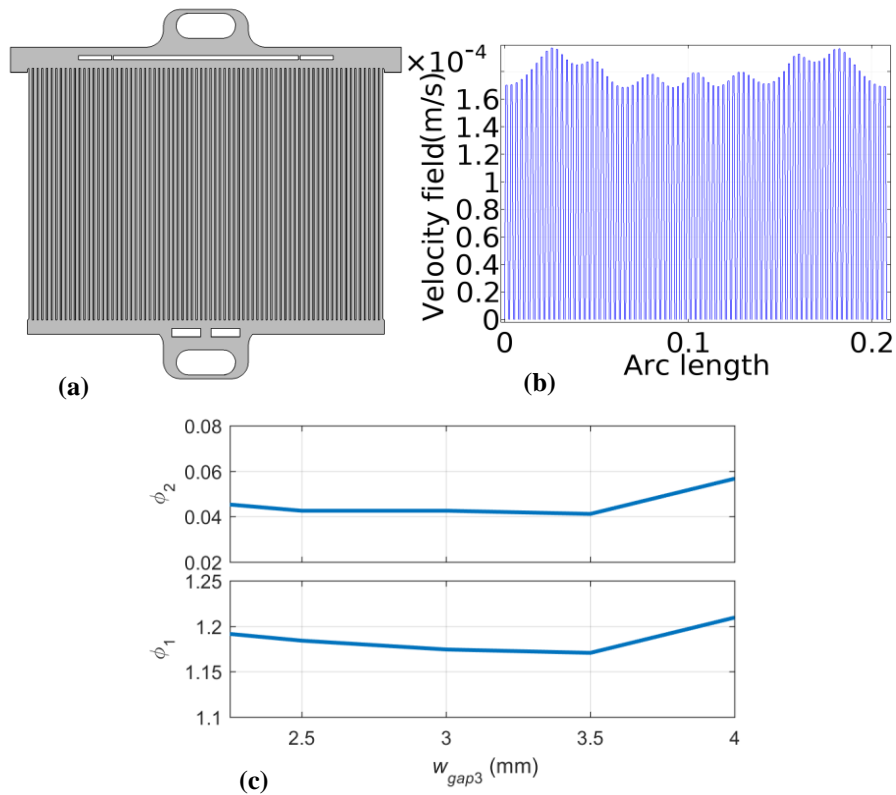As a representative of this final study, the variation of Φ_1 and Φ_2 is demonstrated with

(a) (b)

(c)

FIGURE 3.10: (a) Final configuration, (b) Flow distribution of the final design, (c) Φ_1 and Φ_2 vs w_{gap3} (width of the hole in the outlet baffle).

42

respect to the gap size between the exhaust baffles in Fig. 3.10c for a total length of 4 cm with 5 mm width. The dimensions of the inlet baffle are w_{gap1}=1 mm, d_1=5.5 cm, and d_2=2 cm. The final design achieves Φ_1 and Φ_2 values of 1.17 and 0.041, respectively. This final design is acceptable as the maximum channel-velocity to minimum ratios is within less than 1.2 and the rms value is less than 5%.

The final design shows almost a uniform flow distribution among the channels of the anode flow field. Therefore, it can ensure a uniform flow distribution over the membrane of the cell which is the most important factor in designing the bipolar plates.

3.2. Results of Optimization of Flow Concentration Distribution through Anode Active Area by Including Species Transport

In this section, first an unstructured method is utilized to obtain a uniform distribution of the hydrogen concentration in the active area of the anode domain. Afterward, a sensitivity analysis is used to investigate the effects of the dimensions of the baffles and gaps used in the feed header as well as exit velocity on the uniformity of the distribution of the hydrogen concentration in the anode active area.

First, the optimum design of the previous study (section 3.1) is considered for the anode flow field. Figure 3.11 shows the distribution of the hydrogen mole fraction in this configuration.

This configuration is not an optimum design for the 2-dimensional model since it has high hydrogen starvation region and there is a back flux of nitrogen to the anode inlet. Therefore, the configuration considered for the anode flow field is changed to one indicated in Fig. 3.12. It contains inlet and outlet manifolds; feed and exhaust headers; channels and ribs between the headers; and some baffles in the feed header. Baffles are not used in the exhaust header to prevent having backward flux of the nitrogen to the anode inlet. In this model, the active area includes inlet and exhaust headers in addition to the channels and ribs. Furthermore, GDL is modeled as a connector between channels (ribs) and used instead of the baffles in the feed header, which yields more practical results.
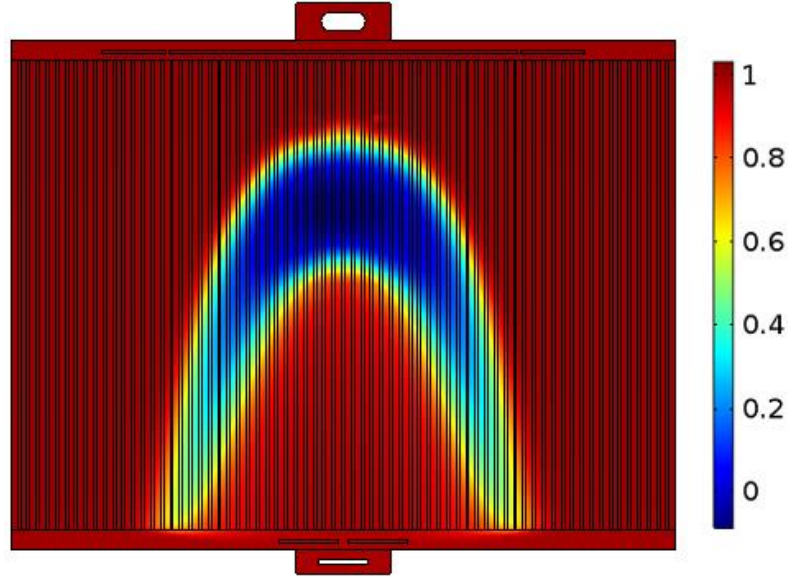
FIGURE 3.11: Distribution of the hydrogen mole fraction in the anode flow field for the optimum design of 3-D model (section 3.1).

The dimensions and positions of the inlet and outlet manifolds and widths of the channels and ribs are kept constant in this study. The inlet manifold is placed at the top and middle of the feed header and the outlet manifold is placed at the bottom and middle of the exhaust header. The exhaust manifold is smaller than the inlet manifold to increase the flow rate of the exhausted flow for a fixed exit velocity and to push more nitrogen to the outlet manifold. The widths of the channels and ribs are set to 2 and 1 mm, respectively. Design variables include the dimensions of the baffles and gaps used in the feed header. There is a central baffle below the inlet manifold and baffles in both its sides. The numbers of the baffles used on each side of the central baffle are equal, and they have the same width. Further, the widths of the gaps between the baffles are the same except the widths of the gaps located at the end of each side between the last baffles and side edges of the feed header. Finally, the number of the baffles on each side (n), width of the gaps between baffles (w_{gb}), width of the side gaps (w_{gs}), and length of the central baffle (d_{cb}) are considered as design variables. Since the length of the feed header is fixed, the length of the baffles does not need to be considered as a design variable, and it can be obtained based on the values of the design variables mentioned above. There is another design variable
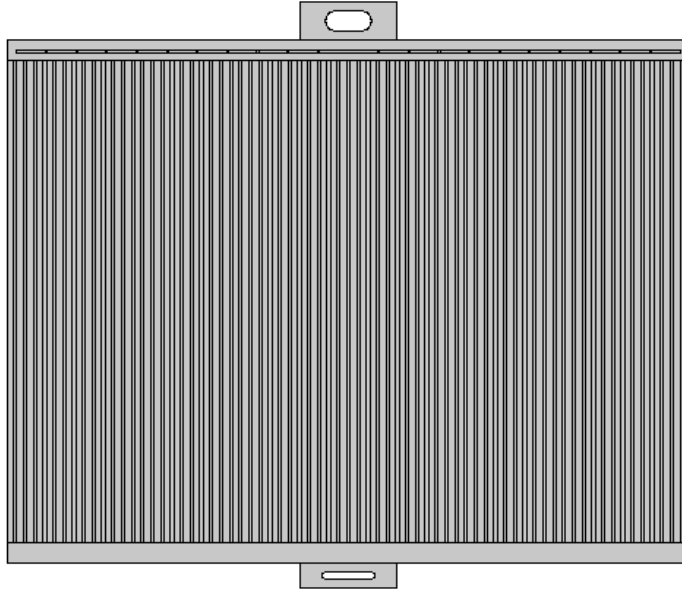
44

FIGURE 3.12: Configuration of the anode flow field considered for the 2-D model.

defined as k_v, which is a coefficient multiplied to the permeance of the nitrogen from the cathode side to specify exit velocity.

An unstructured search is applied to the design variables to obtain the optimum case based on the performance metric, which is defined as the ratio of the area of hydrogen mole fraction less than a certain value between 0.5 and 0.95 divided by the active area, and it is specified as the hydrogen-depletion region ratio, Φ_3. The goal is minimizing Φ_3 while hydrogen utilization is kept greater than 99% (because of the ultra-low stoichiometric flow condition applied to the anode flow).

Figure 3.13 shows the distribution of the hydrogen mole fraction in the anode flow field for the optimum case. Blue regions are hydrogen-depleted regions that show a lack of hydrogen in these regions. For this configuration, design variables are: $n=10$, $w_{gb}=0.5$ mm, $w_{gs}=3$ mm, $d_{cb}=1.9$ cm, and $k_v=4$. The hydrogen-depletion region ratio, or Φ_3, for the hydrogen mole fraction less than 0.95 and 0.9 are 0.031 and 0.0016, respectively. Further, Φ_3 is almost 0 for a hydrogen mole fraction of less than 0.9.

In order to observe the effect of the design variables on the performance metric, sensitivity analysis is used for each design variable while others are kept constant and equal to their optimum values.
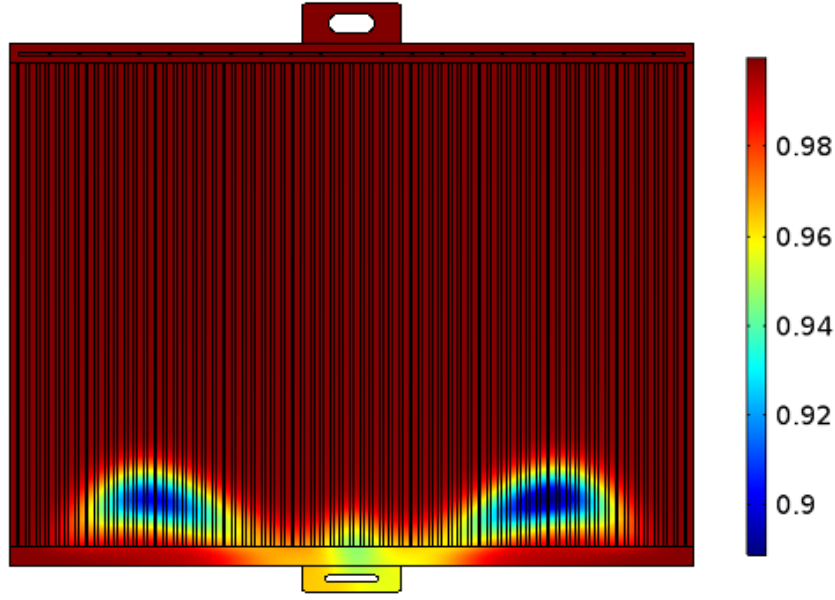
FIGURE 3.13: Distribution of the hydrogen mole fraction in the anode flow field for the optimum design of the 2-D model.

3.2.1. Effects of Number of Baffles

In this section, the hydrogen-depletion region ratio is studied as a function of the number of baffles on each side of the central baffle. Other design variables are kept constant and equal to their optimum values as w_{gb}=0.5 mm, w_{gs}=3 mm, d_{cb}=1.9 cm, and k_v=4. The number of baffles (n) is varied from 2 to 22, and Φ_3 is studied for hydrogen mole fractions from 0.5 to 0.95, as illustrated in Fig. 3.14. For all cases, Φ_3 decreases sharply at first and then decreases gradually and hits the minimum for n=10, increases after this point with the increases in the number of baffles. Changes in Φ_3 are low for the increase in the number of baffles greater than 13, and Φ_3 is not studied for n greater than 22 since they are not practical and means there will be about one gap per channel. Further, the same behavior is observed for the hydrogen mole fraction of less than 0.5, and these cases are not displayed.
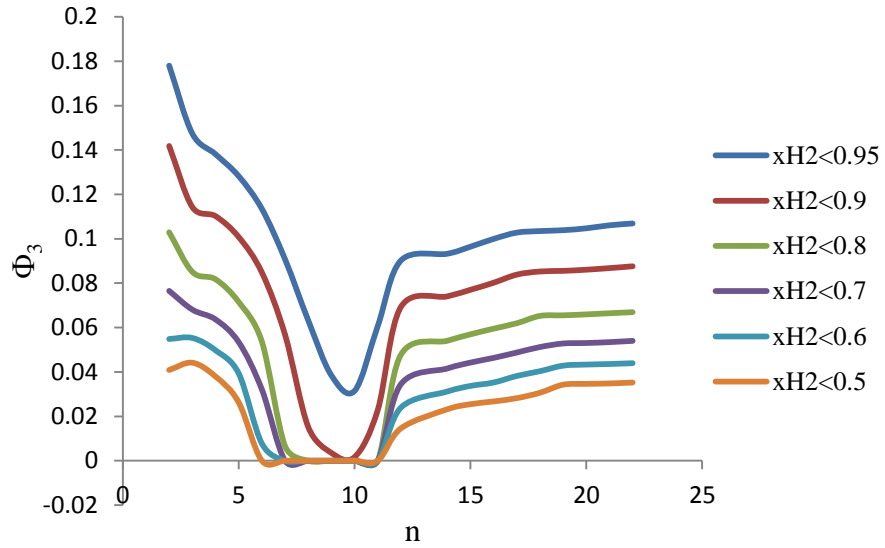
FIGURE 3.14: Effects of the number of baffles.

3.2.2. Effects of Width of Gaps between Baffles

The hydrogen-depletion region ratio, Φ_3, is analyzed for different values of the width of the gaps between the baffles, as illustrated in Fig. 3.15. Other design variables are fixed to their optimum values as $n=10$, $w_{gs}=3$ mm, $d_{cb}=1.9$ cm, and $k_v=4$. The widths of the gaps
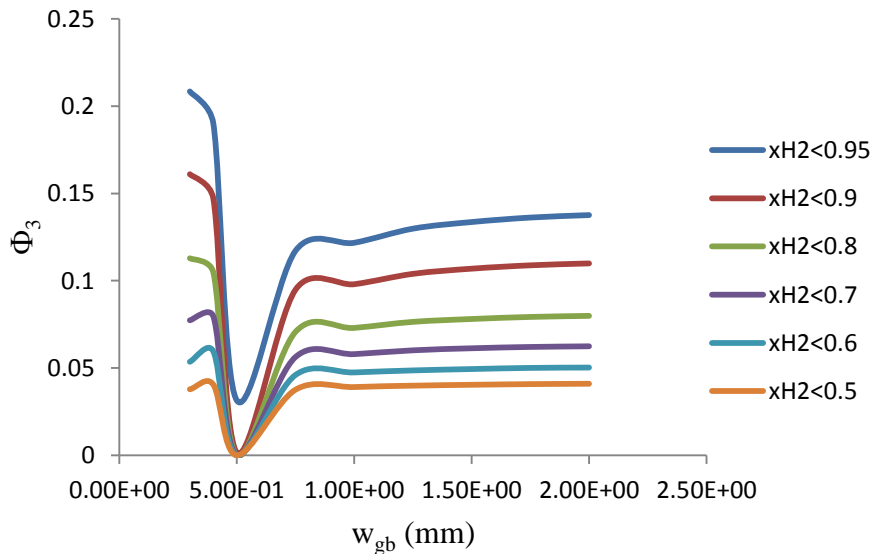

FIGURE 3.15: Effects of the width of gaps between the baffles.

(w_{gb}) vary between 0.3 and 2 mm, and Φ_3 is studied for hydrogen mole fractions from 0.5 to 0.95. The minimum value of Φ_3 is observed for w_{gb}=0.5 mm for all cases, and Φ_3 decreases sharply for the low values of the width of the gaps, reaches the minimum, and then increases rapidly until w_{gb}=0.75 mm, and after this point, it almost remains constant as the width of the gaps increases. In addition, Φ_3 has the same behavior for other cases which have a hydrogen mole fraction of less than 0.5, and these cases are not shown.

3.2.3. Effects of Width of Side Gaps

In this section, the effect of the widths of the side gaps on the hydrogen-depletion region ratio is investigated. The reason that the width of the side gaps is different from the width of the gaps between the baffles is to provide more flow to the channels close to the edges. The widths of the side gaps range from 1 mm to 1.5 cm and the hydrogen-depletion region ratio is investigated as a function of the widths changes of the side gaps, as indicated in Fig. 3.16. Other design variables are fixed to their optimum values as n=10, w_{gb}=0.5 mm, d_{cb}=1.9 cm, and k_v=4. The minimum of the hydrogen-depletion region ratio, Φ_3, is obtained for the w_{gs}=3 mm for all cases of the hydrogen mole fractions from 0.5 to 0.95.
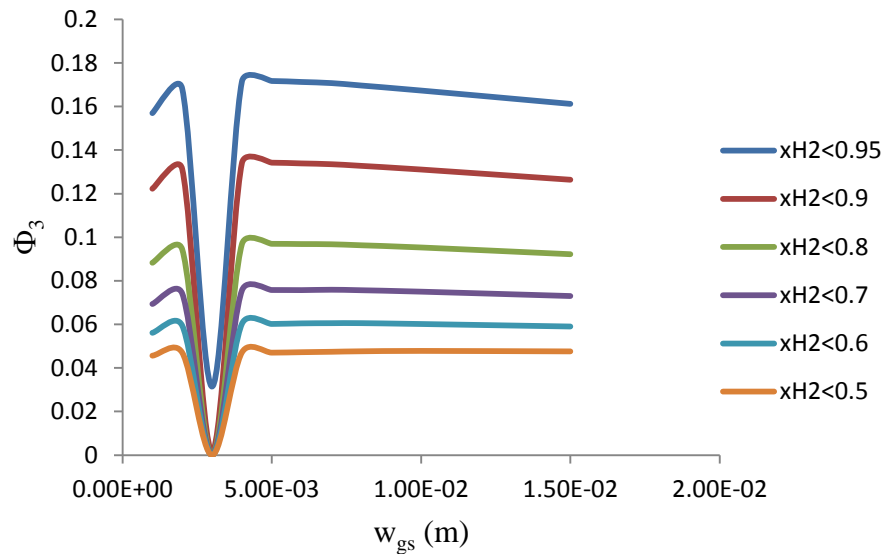

FIGURE 3.16: Effects of the width of side gaps.

48

This result shows that width of the side-gabs has to be larger than the width of the gaps used between the baffles. There is an increase in the Φ_3 at the beginning of the width of the side gaps interval at $w_{gs}=2$ mm. However, after this point, Φ_3 decreases and passes the minimum point at $w_{gs}=3$ mm and increases after this point until $w_{gs}=4$ mm and remains almost constant with the changes in the width of the side gaps for all cases. Further, Φ_3 is studied for the values of the hydrogen mole fraction less than 0.5 and it has the same behavior for those cases but they are not displayed.

3.2.4. Effects of Length of Central Baffle

The last design variable which is related to the geometry of the feed header configuration is the length of the central baffle. This central baffle is important in providing flow for the channels far from the center and preventing the maximum flow in the central channels. Therefore, this baffle is designed separately and its length is different than the length of the baffles on each side. Here, the hydrogen-depletion region ratio is studied as a function of the changes of the length of the central baffle, while other design variables are kept constant and equal to their optimum values as $n=10$, $w_{gb}=0.5$ mm, $w_{gs}=3$ mm, and $k_v=4$. Figure 3.17 shows the behavior of Φ_3 versus d_{cb} for hydrogen mole fractions less than
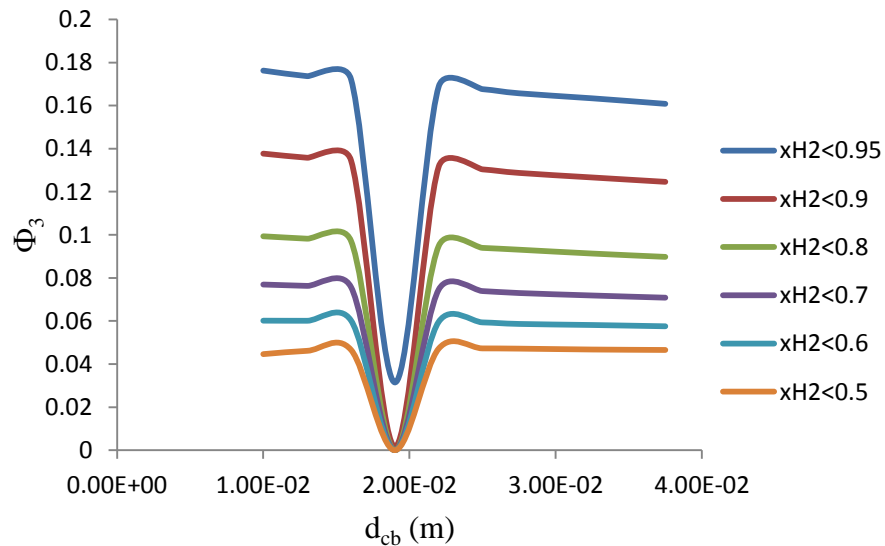

FIGURE 3.17: Effects of the length of central baffle.

0.5 to 0.95. In all cases minimum of Φ_3 is observed for d_{cb}=1.9 cm, Φ_3 is almost constant at the beginning of the length of the central baffle interval, then decreases and passes the optimum point, increases until d_{cb}=2.2 cm, and after this point, it remains almost constant until the end of the interval of the length of the central baffle. As previous cases, this study includes the hydrogen mole fractions less than 0.5 but they are not showed here since they have the same behavior.

3.2.5. Effects of Coefficient of Exit Velocity

The only design variable which is not related to the dimension of the feed header configuration is k_v. This variable is used to determine the exit velocity at the outlet manifold, and it is related to the amount of flow supplied to the anode channels. Exit velocity is equal to the permeance of the nitrogen that comes from the cathode side times this coefficient, k_v. This velocity coefficient cannot be changed freely since hydrogen utilization is depending on its value and ultra-low stoichiometric (ULS) flow condition is desired. Thus, this coefficient is increased to the values which their hydrogen utilizations are greater than 99% to keep the ULS flow condition.
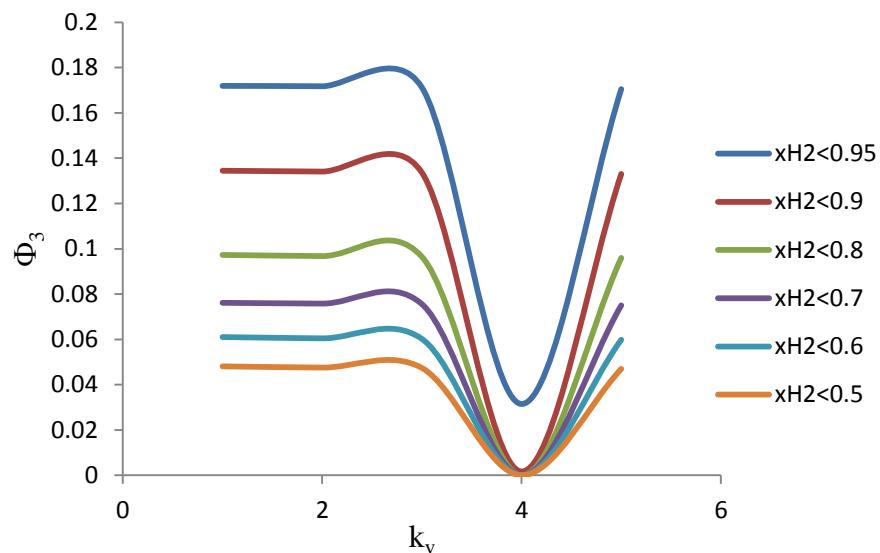

FIGURE 3.18: Effects of the coefficient of exit velocity.

Figure 3.18 shows the effect of the coefficient of exit velocity, k_v, on the hydrogen-depletion region ratio, Φ_3. Velocity coefficient varies from 1 to 5, and higher values are not studied since their hydrogen utilizations are less than 99%, as demonstrated in Fig. 3.19. The value of Φ_3 is constant for k_v between 1 and 2, then it decreases and passes the minimum at $k_v=4$, and after this point, it increases for all cases. In this analysis, other design variables are fixed to their optimum values as $n=10$, $w_{gb}=0.5$ mm, $w_{gs}=3$ mm, $d_{cb}=1.9$ cm. Furthermore, this analysis includes the hydrogen mole fractions less than 0.5 and they have the same behavior, however, their results are not displayed.

By taking all above-mentioned analysis into consideration, the design variables of the optimum configuration of the anode flow field are $n=10$, $w_{gb}=0.5$ mm, $w_{gs}=3$ mm, $d_{cb}=1.9$ cm, and $k_v=4$. The final design has a uniform hydrogen concentration in the active area of the anode flow field. Therefore, it can ensure a uniform hydrogen distribution over the anode side of the membrane which is the most important factor in designing the bipolar plates.
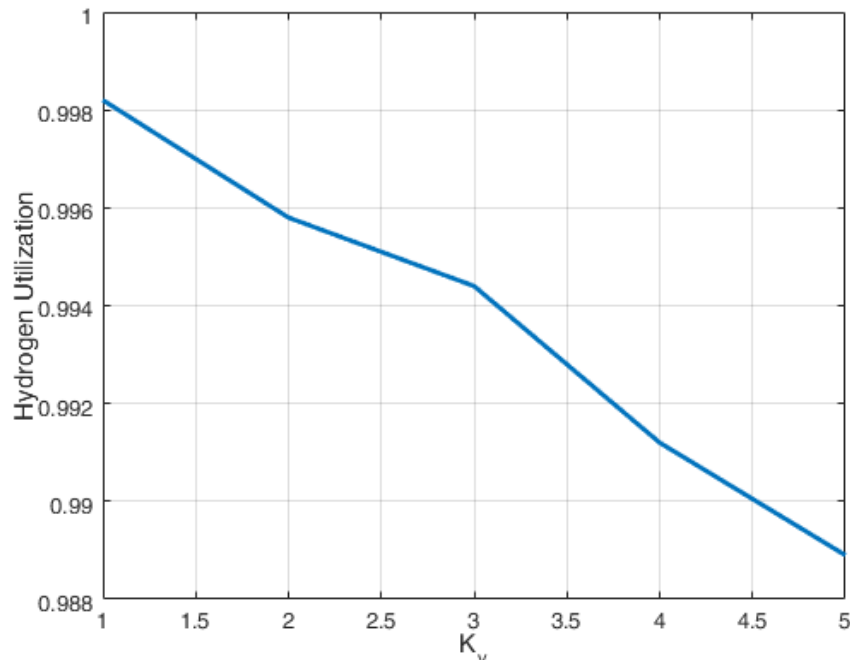

FIGURE 3.19: Hydrogen utilization versus the coefficient of exit velocity.

3.3. Results of Cathode Flow Field Design

In this section, designing a configuration for the cathode flow field is investigated. This design has to provide enough pressure drop between the inlet and outlet manifolds to remove excess water generated at the cathode side, and reduce the parasitic power used to pressurize the air supplied to the cathode inlet. Unlike the models used for the anode flow field, a high stoichiometric flow condition can be used in the cathode flow field since air is supplied to the cathode inlet manifold. The serpentine channel flow fields are the only candidate for the mentioned design criteria, and the goal is finding a configuration which has a pressure drop within 30% of the output power of the cell.

Figure 3.20 shows the geometry used for the cathode flow field. The important design dimensions are the number of the channels, n_{chc}; and the widths of the channels and ribs, w_{chc} and w_{rc}, respectively. These dimensions are dependent and they are specified based on the active area dimensions, i.e. by changing the value of one of them others have to be changed to confine channels in the active area. Because of this dependency, a grid-type search with respect to n_{chc}, w_{chc}, and w_{rc} is not possible, and an unstructured search is used
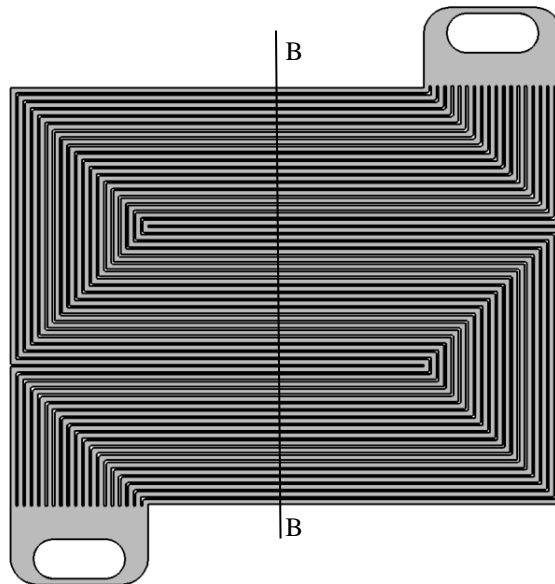

FIGURE 3.20: Serpentine flow field configuration used for the cathode domain; section B-B located at the middle of the channels.

to find a configuration which provides a sufficient amount of the pressure drop between the inlet and outlet manifolds. Further, it has to be mentioned that the positions and dimensions of the inlet and outlet manifolds are fixed, and they are not changed during this search. The final design is obtained for n_{chc}=19, w_{chc}=2 mm and w_{rc}=0.8 mm. Figure 3.21 indicates the pressure distribution in the cathode flow field for the final design. Pressure difference is about 16 kPa for this design, which is high enough to push the water droplets formed in the channels to the outlet manifold and low enough to reduce the parasitic power needed to pressurize the air supplied to the cathode inlet manifold.

Figure 3.22a shows the distribution of the magnitude of the flow velocity in the cathode flow field. Flow velocity varies between 3 and 5 m/s in the cathode channels, as a result of the pressure difference between the inlet and outlet manifolds. Further, this figure indicates low velocity gradients in the flow from the inlet to the outlet, which is because of an appropriate length of the channels used in this design. Figure 3.22b illustrates the distribution of the magnitude of the flow velocity across the B-B section, which is at the center of both the length and depth of the cathode channels. This figure shows that there is a uniform flow distribution in the cathode flow field, and a uniform flow is supplied to the cathode GDL and subsequently to its catalyst layer (CL) to take part in the reaction. In this
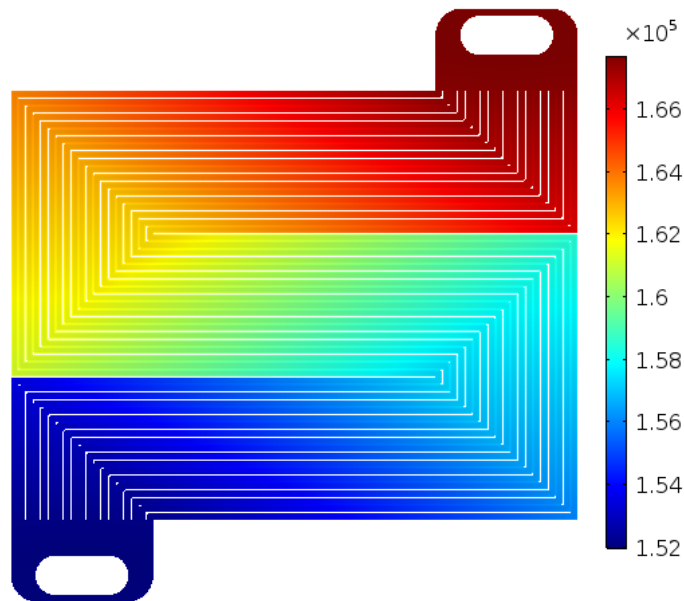

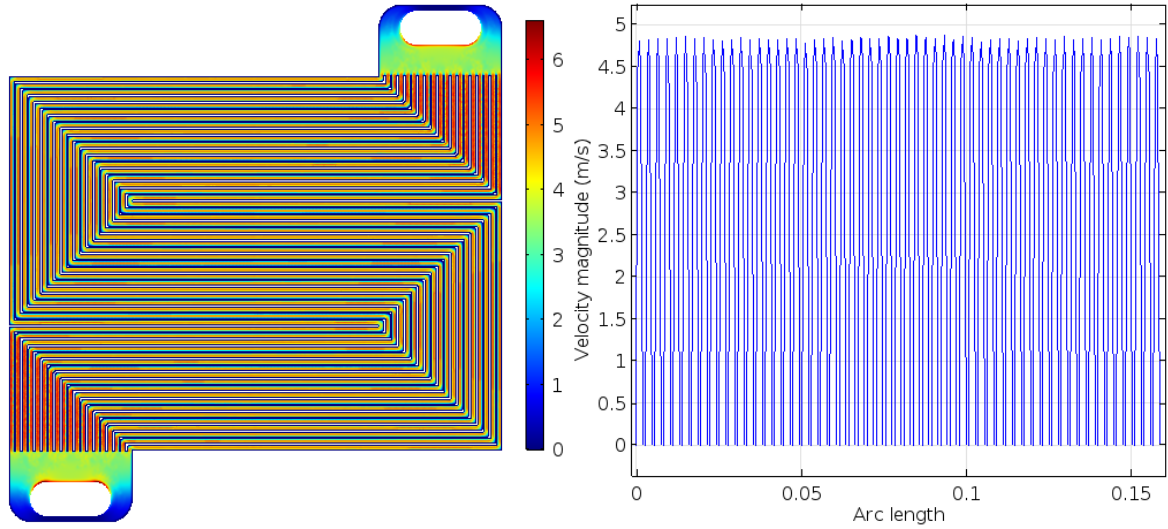FIGURE 3.21: Pressure distribution of the cathode flow field.

FIGURE 3.22: (a) Velocity distribution of the cathode flow field; (b) Velocity distribution across the B-B section.

design, the pressure drop is 16 kPa which is less than 30% of the cell output power, thus this configuration satisfies the design criteria.

3.4. Results of Cooling Flow Field Design

In this section, designing a configuration for the cooling flow field is investigated. A parallel serpentine channel flow field like the one used for the cathode flow field is used here, as shown in Fig. 3.23. The cooling liquid is water, which has a high thermal capacity and is the most common liquid used for cooling the high power (automotive) PEM fuel cells. The goal of this study is to find a configuration for the cooling flow field which gives a uniform temperature distribution over the cooling plate with the index of uniform temperature less than 3 °C.

The design variables are the number of the channels (n_{chw}), width of the channels (w_{chw}), width of the ribs (w_{rw}), depth of the channels (h_w), and pressure difference between the inlet and outlet manifolds (ΔP). These variables, except the pressure difference, are related to the dimensions of the cooling flow field, and they are dependent variables which determined based on the active area dimensions, which is 16 by 21 cm. Dimensions and
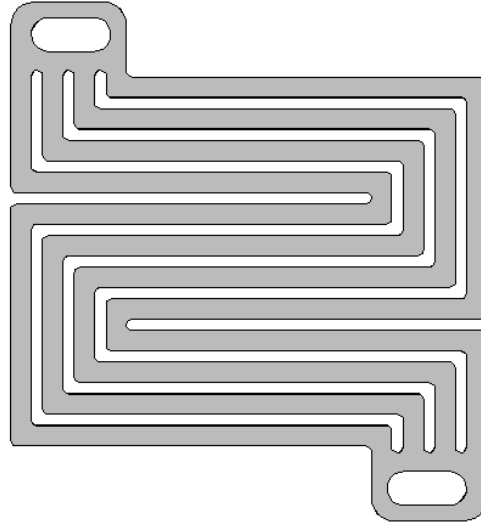
54

FIGURE 3.23: Serpentine flow field configuration used for the cooling domain.

positions of the inlet and outlet manifolds are fixed and they are not included in the flow field analysis. The goal of this study is to investigate the effect of the mentioned design variables on the temperature distribution in the cooling field and optimize the value of the index of uniform temperature (IUT), which is the difference between the maximum and minimum temperatures in the cooling plate.

3.4.1. Effects of Width, Height, and Number of Channels and Ribs

Figure 3.24 demonstrates the effect of the number of the channels and widths of the channels and ribs on the temperature distribution in the cooling field while the depth of the channels and pressure difference are kept constant as h_w=2 mm and ΔP=1 kPa, respectively. In cases a, b and c the number of channels are fixed and the widths of the channels and ribs are investigated. By increasing the channels widths and decreasing the ribs widths for a constant number of channels (n=3), the IUT value is reduced from 6 to 4 °C. However, this improved configuration, case c, is not applicable since the width of the ribs for this case is 4 mm while the width of the channels is 14.5 mm, which is about 3.5 times greater than the width of the ribs and make the ribs weaker than needed to be able to support the channels in the cell configuration. Therefore, in the next trial (case d) the number of channels is
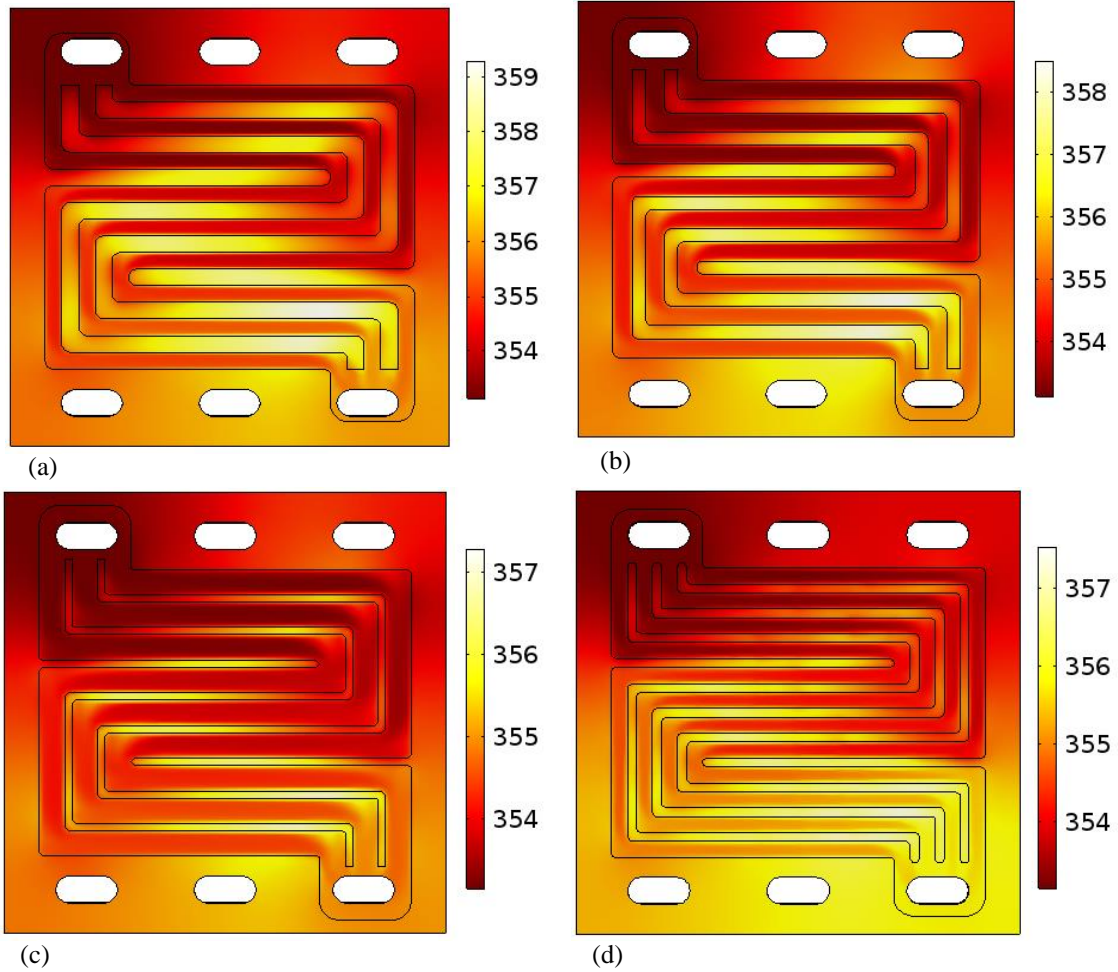
FIGURE 3.24: Temperature distribution in the cooling domain; (a) n_{chw} =3, w_{chw}=9.5mm and w_{rw}=9.5mm; (b) n_{chw} =3, w_{chw}=11mm and w_{rw}=7.5mm; (c) n_{chw} =3, w_{chw}=14.5mm and w_{rw}=4mm; (d) n_{chw} =4, w_{chw}=9mm and w_{rw}=5mm; in all cases ΔP=1kPa and h_w=2mm.

increased to 4 to obtain a more reasonable configuration. The widths of the channels and ribs are 9 and 5 mm, respectively for this case, and the IUT value is about 4 °C. A further increase in the number of channels is not investigated since the cooling domain is expected to remain as simple as possible.

The next analysis is based on the depth of the water channels, as illustrated in Fig. 3.25. The depth of the channels is varied from 1 to 5 mm in the best case obtained in the previous analysis, in which its dimensions are n_{chw}=4, w_{chw}=9 mm, and w_{rw}=5 mm and its pressure difference is fixed to ΔP=1 kPa. This analysis indicates that increasing the depth of the channels will not improve the temperature distribution sufficiently since the temperature difference is improved less than 6% while the depth of the channels increases

(a)   (b)
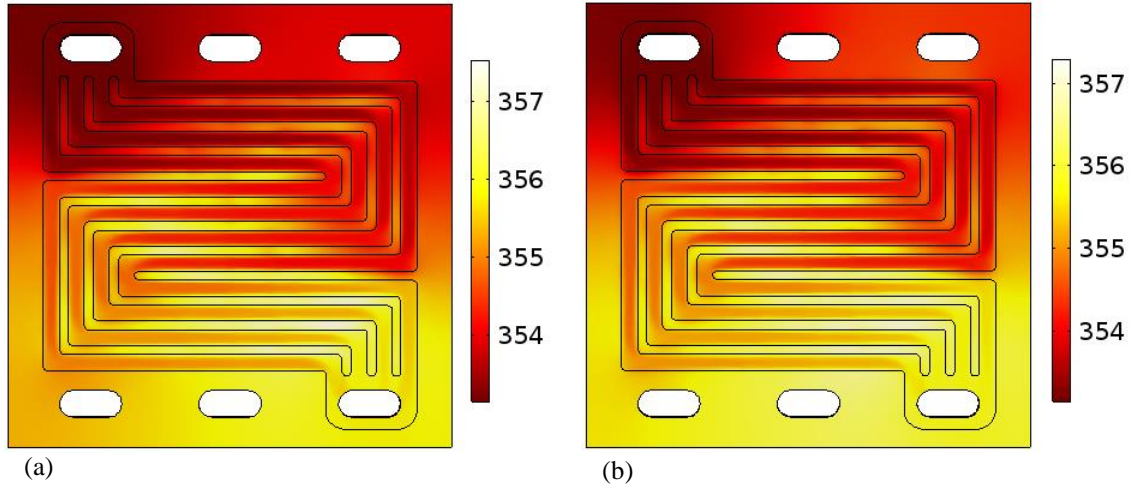
FIGURE 3.25: Temperature distribution in the cooling domain for n_{chw} =4, w_{chw}=9mm, w_{rw}=5mm and ΔP=1kPa; (a) h_w=1mm; (b) h_w=5mm.

five times greater than the basic depth of the channels (h_w=1 mm). Thus, the depth of the channels can be removed from the design variables and it is fixed at 2 mm.

3.4.2. Effects of Pressure Drop

The final analysis investigates the effects of the pressure difference between inlet and outlet manifolds on the temperature distribution and the temperature difference (IUT). The dimensions of the design used in this analysis are n_{chw}=4, w_{chw}=9 mm, w_{rw}=5 mm, and h_w=2
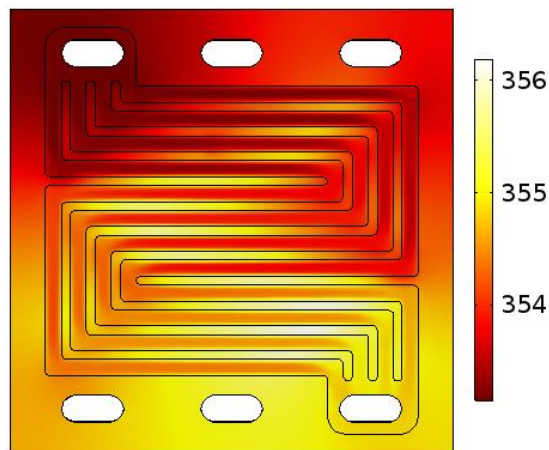
FIGURE 3.26: Temperature distribution in the cooling domain for n_{chw} =4, w_{chw}=9mm, w_{rw}=5mm, h_w=2mm and ΔP=2kPa.

57

mm. Figure 3.26 shows the temperature distribution of the mentioned case for a pressure difference equal to 2 kPa. The temperature difference, value of IUT, for this design is less than 3 °C, which is small enough to be consistent with the mentioned design criteria of the cooling domain. Further increases in the pressure difference between the inlet and outlet manifolds are not investigated since they yield higher parasitic power supplied to the water pump.

3.5. Results of Liquid Water Transport and Distribution through Channels and GDLs

In this section, the results of the one-dimensional model of the liquid water transport and distribution through the anode and cathode channels and their GDLs are compared with the experimental data provided by [65]. Two experimental data sets of different operation conditions are used in the comparisons. A dead-ended condition is applied to the anode side with DEA transients that take 900 s between purges.
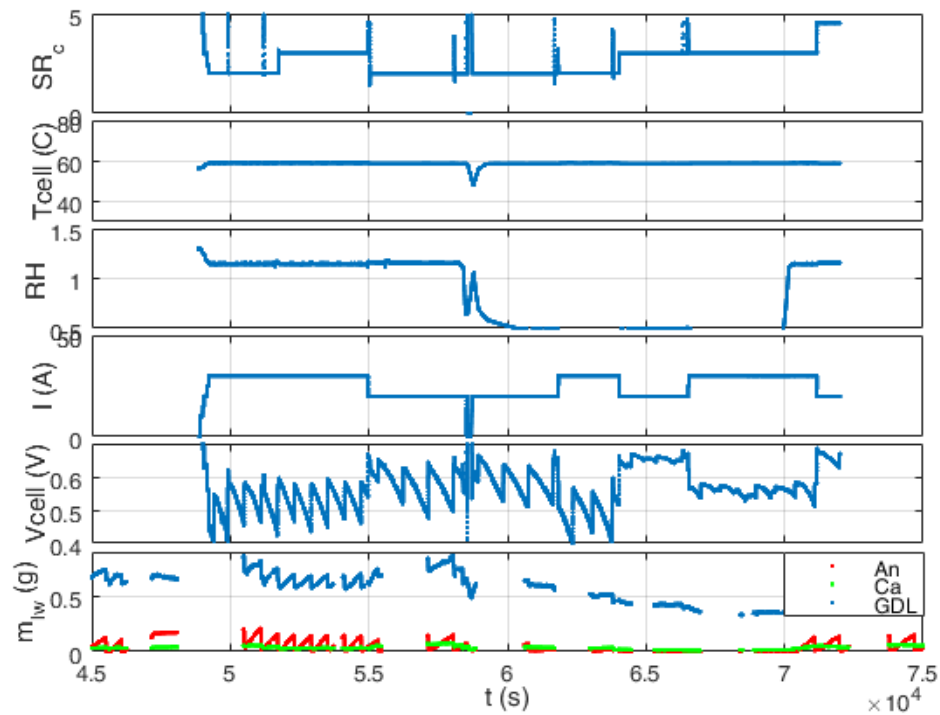
FIGURE 3.27: First set of the experimental data; data for relative humidity more than one can be achieved.

58

Figure 3.27 shows the first experimental data set for various operation conditions during the time span between 45,000 and 75,000 s. The first four subplots indicate the operation condition as the stoichiometric ratio of the air supplied to the cathode inlet (SR_c), the operation temperature of the cell (T_{cell}), the relative humidity of the flows provided to the anode and cathode inlets (RH), and the load current of the cell (I). The cathode flow stoichiometry ratio varies between 0.5 and values larger than one, the operation temperature is kept constant as 60 °C, the relative humidity varies from 0.5 to 1.2, and the load current changes between 20 and 30 A during this set of experimental data. The last two subplots illustrate the results of the experiment as the cell voltage (V_{cell}), and the liquid water masses (m_{lw}) in the anode and cathode channels and their GDLs. Liquid water masses in the anode and cathode GDLs are considered together, i.e. the mass of the GDL liquid water in the results is the sum of the liquid water masses in the anode and cathode GDLs. These results are periodic because of the periodic purges at the anode exit. Figure 3.28 has the same layout as mentioned above, and its only difference is due to its relative humidity which is constant and less than one, which is called dry operation.
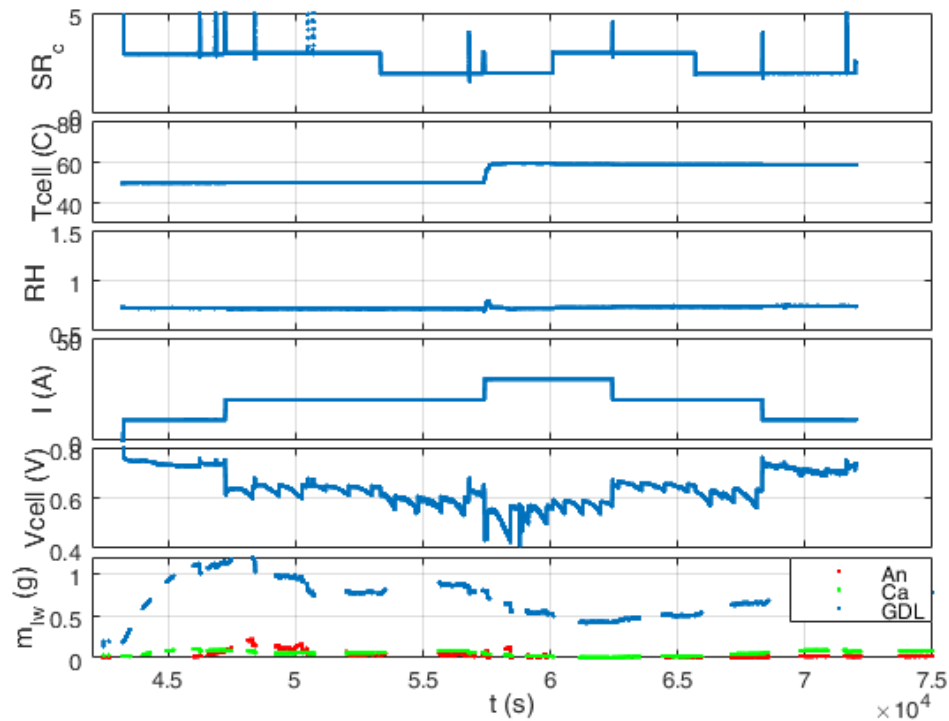
FIGURE 3.28: Second set of the experimental data; relative humidity is less than one.

Finding an appropriate time interval without any sudden changes in the operation condition and with a sufficient amount of results for comparison is important. In Fig. 3.27, the chosen time interval is from 57,170 to 58,070 s, since in addition to satisfying the mentioned conditions, the relative humidity of this interval is more than one and different than the relative humidity of the next set of data, which is constant and less than one. The chosen time interval for the next set of experimental data, shown in Fig. 3.28, is between 61,150 and 62,050 s. Based on these two time interval selections, there are two sets of operation conditions: $RH = 1.15$, $SR_c = 2$, $I = 20$ A, and $T_{cell} = 60$ °C; and $RH = 0.75$, $SR_c = 3$, $I = 30$ A, and $T_{cell} = 60$ °C.

The mentioned operation conditions are applied to the one-dimensional model of the liquid water transport and distribution through the anode and cathode channels and their GDLs; and the results of the model are compared with the results of the experimental data. Figure 3.29 demonstrates a comparison between the experimental data and the model results for the first operation condition, $RH = 1.15$, $SR_c = 2$, $I = 20$ A, and $T_{cell} = 60$ °C. The first three subplots indicate a comparison between the masses of the liquid water in the

FIGURE 3.29: Comparison between the results of the model and experimental data for the operation condition: RH=1.15, SR$_c$=2, I=20 A, and T$_{cell}$=60 °C.

60

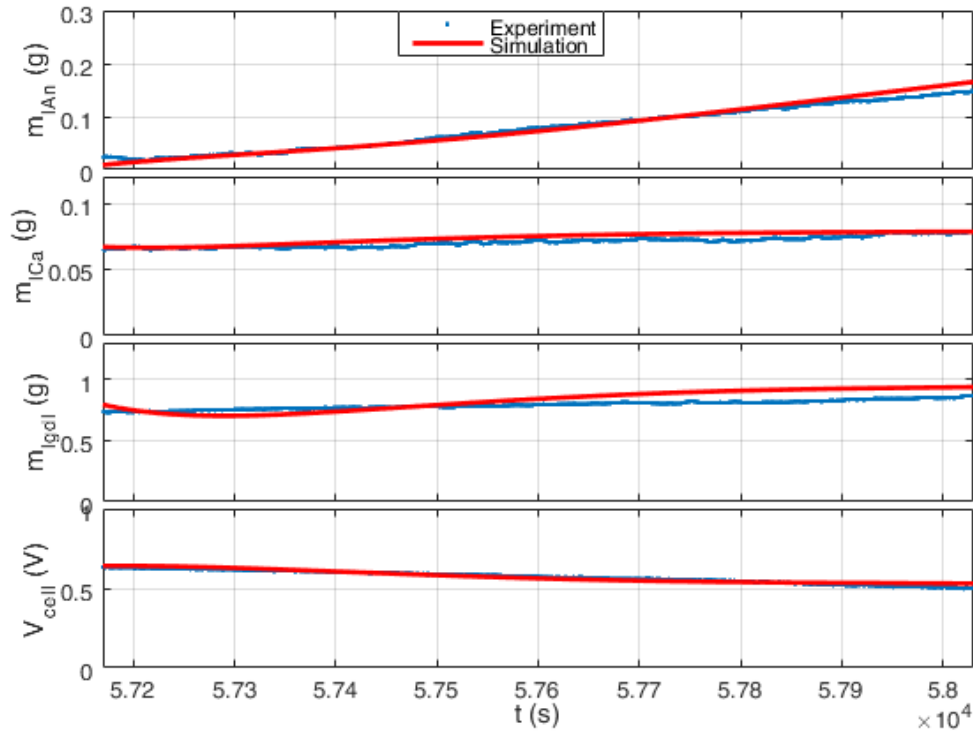anode and cathode channels and their GDLs, respectively; and the last subplot illustrates a comparison between the cell voltages obtained from the model and experimental data. In all subplots, the results of the experimental data and one-dimensional model are indicated with blue dots and red curves, respectively. The results of the model agree reasonably with the measured data of the experiment, and the only problem is in the results of the mass of the liquid water in the GDLs. Based on the experimental data, it is expected that the liquid water in the channels and GDLs are removed during each purge time and their corresponding liquid water start increasing in the next transient. However, the mass of the liquid water in the GDLs is decreased until about 100 s after each purge and start increasing afterward in the results of the model. Nevertheless, the values of the model-predicted liquid water in the GDLs are close to their corresponding values in the experimental data.

Figure 3.30 shows a comparison between the results of the one-dimensional model and the experimental data for the second operation condition, $RH = 0.75$, $SR_c = 3$, $I = 30$ A, and $T_{cell} = 60$ °C. This figure layout is similar to the one explained for the previous figure. Since the relative humidity in this operation condition is less than the relative humidity of
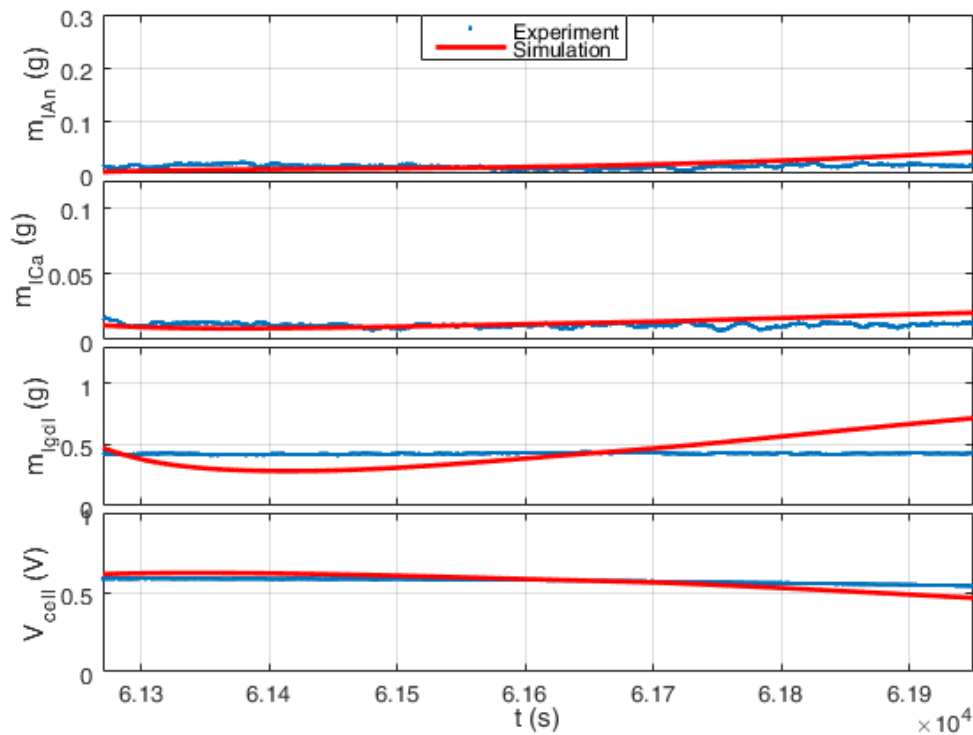
FIGURE 3.30: Comparison between the results of the model and experimental data for the operation condition: RH=0.75, SR$_c$=3, I=30 A, and T$_{cell}$=60 °C.

61

the previous operation condition, the liquid water in the channels and GDLs is less here and remains almost constant. The model-predicted voltage and liquid water in the channels agree well with the experimental data. However, the liquid water in the GDLs predicted by the model is not matched accurately with the measured data of the experiment; there is the same problem as the one mentioned for the previous case.

The most important factor in defining the time period of DEA transients between the purges is based on the distribution of the mole fractions of hydrogen and nitrogen along the length of the anode channel during each transient. Figure 3.31 shows the distribution of the mole fractions of hydrogen and nitrogen, and the current density along the length of the anode channel for three times: after a purge, at the midcycle, and before the next purge. At the first snapshot, $t = 50$ s, hydrogen and nitrogen mole fractions and the current density are distributed uniformly along the length of the channel. As time passed after each purge, the hydrogen mole fraction and current density decrease along the length of the channel and the
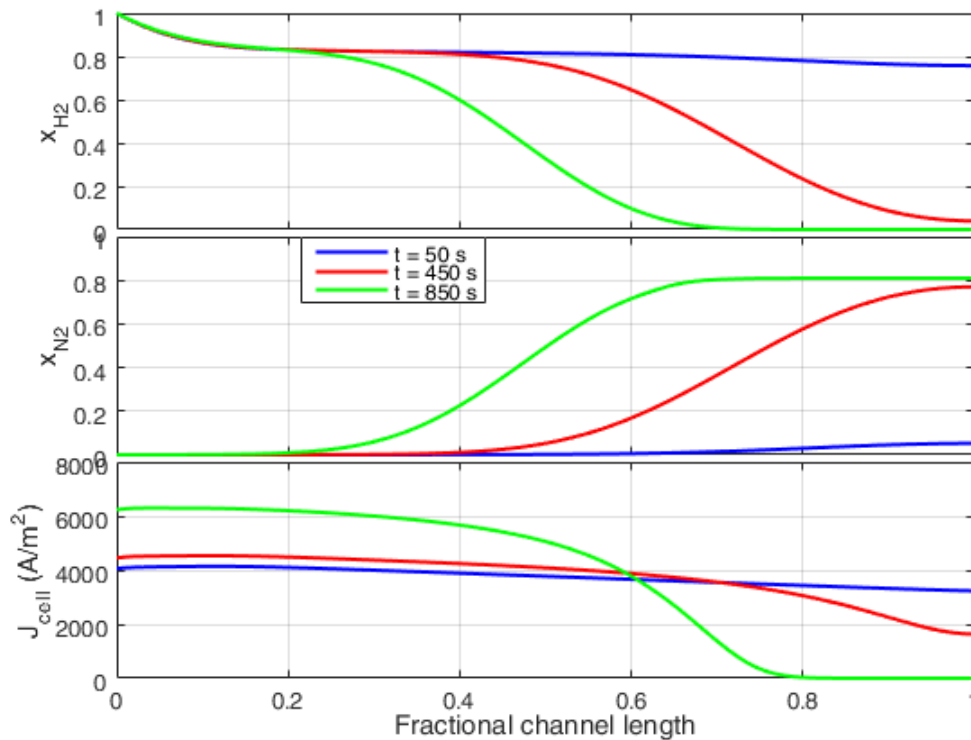
FIGURE 3.31: Distribution of the hydrogen and nitrogen mole fractions, and current density along the length of the anode channel for three times: after a purge, $t = 50$ s; midcycle, $t = 450$ s; and before the next purge, $t = 850$ s.

62

nitrogen mole fraction increases along the channel, which is because of the nitrogen accumulation and subsequently hydrogen starvation in the anode channel. Hydrogen convective velocity at the anode inlet pushes the accumulated nitrogen to the end of the anode channel where hydrogen starvation occurs. The last snapshot, $t = 850$ s, indicates severe hydrogen starvation in the anode channel, which leads to a hydrogen starved region covering about 30% of the channel. Hydrogen starvation causes the local current density to fall to zero and reduce the performance of the cell.

4. CONCLUSION

In this study, the geometry of the flow fields used in the anode, cathode, and cooling sides of a large PEM fuel cell with high hydrogen utilization, which is used in the automotive (high power) applications, are designed and optimized. Furthermore, species and liquid water transport and distribution through the anode and cathode flow fields and their GDLs are modeled.

In section 2.1, a three-dimensional CFD model is used to investigate the flow distribution in the flow field, especially in the channels, of the anode domain. Ultra-low stoichiometric (ULS) flow condition is applied to the anode outlet manifold based on the permeance of nitrogen diffuses through the membrane and reaches to the anode active area. Species and liquid water transport through the membrane are not included in this model. Because of the ULS flow condition in the anode flow field, Reynolds number of the flow in the anode channels is very low and Stokes (Creeping) flow equations can be solved to find the flow distribution in this model. Topologies of the baffles used in the feed and exhaust headers as well as dimensions of the channels and ribs are analyzed to obtain a uniform flow distribution among the channels. Final configuration consists of three baffles in the feed header, two baffles in the exhaust header, and its channel-to-rib width ratio is 2.7:1. In the final design, the maximum to minimum ratio and rms value of the flow velocity in the channels are less than 1.2 and 5%, respectively.

In section 2.2, a two-dimensional CFD model of the anode domain with species transport through the membrane is used to analyze the nitrogen accumulation (blanketing phenomena) and hydrogen concentration in the anode active area. ULS flow condition based on the permeance of nitrogen that comes to the anode active area is considered for the flow in the anode flow field, similar to the condition used in the previous model. The effect of the water vapor and liquid water transport through the membrane is neglected in this model. Stokes flow equations are used to model the flow distribution in the anode flow

field since Reynolds number is low, Maxwell-Stefan equations are used to model the species transport through the membrane, and a voltage model is developed to analyze the distribution of the current density and hydrogen consumption rate in the anode domain, and its equations are coupled to the Maxwell-Stefan equations. The final design of the previous model is not optimum in this study and it has a back flux of the nitrogen to the anode inlet. Thus, the baffles in the exhaust header are removed to prevent the back flux of the nitrogen to the anode inlet, and configurations of the baffles in the feed header are analyzed to obtain a uniform distribution of the hydrogen concentration in the anode active area. The final design consists of ten baffles on each side of the central baffle, and its channel-to-rib width ratio is 2:1. In this final design, the hydrogen-depletion region ratio is within 0.2% for the hydrogen mole fraction less than 0.9.

In section 2.3, a three-dimensional CFD model is used to analyze the distributions of the flow velocity and pressure in the cathode flow field. Serpentine channel flow field is considered for the cathode domain, the stoichiometric ratio of the flow is set to a value sufficiently larger than one, and constant mass flow rate and pressure are specified at the inlet and outlet manifolds, respectively. An unstructured search is utilized to find an optimum design for the cathode flow field with a sufficient number of the channels and their dimensions; and subsequently adequate pressure drop to remove the water formed in the cathode side, minimize the parasite power needed to pressurize the air supplied to the cathode inlet manifold, and minimize the gradient of the flow concentration from the inlet to the outlet. The final design has a pressure drop about 30% of the output power of the cell and a uniform flow gradient through the channels.

In section 2.4, a three-dimensional CFD model is used to investigate the distribution of the flow velocity and pressure in the cooling flow field, and the temperature distribution in the cooling domain. Serpentine channel flow field is used for the cooling domain, similar to the cathode flow field. A sufficient pressure difference is applied to the inlet and outlet manifolds, a constant temperature is set to the inlet manifold, and a heat flux is specified on the active area of the cooling flow field to simulate the effect of the heat generated in the active area of the cathode flow field. Dimensions of the channels and ribs as well as the pressure difference between the inlet and outlet manifolds are varied to obtain a uniform temperature distribution in the cooling plate. The final design has a uniform temperature

distribution with the index of uniform temperature (IUT), which is defined as the temperature difference in the cooling domain, less than 3 °C.

In section 2.5, a one-dimensional CFD model of the species and liquid water transport and distribution through the anode and cathode channels and their GDLs is investigated and its results are compared with the experimental data sets. Maxwell-Stefan equations are solved to analyze the distribution and transport of the species through the channels and GDLs. Furthermore, voltage and liquid models are developed and coupled to the Maxwell-Stefan equations to add the reactions kinetics and liquid water distribution and transport through the channels and GDLs, respectively. Results of this model predict the cell voltage and liquid water in the anode and cathode channels with high accuracy. The model-predicted liquid water in the GDLs agrees reasonably with the experimental data, however, there is a difference between them after each purge.

Some future works are suggested as follows:

- Design and optimizing a serpentine flow field for the anode side to improve water removal from the cell.
- Adding the cathode side and water vapor species to the two-dimensional model of the anode side.
- Developing the two-dimensional model of the anode side to a three-dimensional model of the anode and cathode sides.
- Including the anode and cathode catalyst layers (CLs) and micro porous layers (MPLs) in the one-dimensional model of the liquid water simulation.
- Developing the one-dimensional model to a two-dimensional model, and subsequently a three-dimensional model by considering all components of the cell.
- Performing experiments to confirm the effeteness of the designs.

REFERENCES

[1]   Al-Baghdadi, M. A. S. (2013). PEM Fuel Cells: Fundamentals, Modeling, and Applications. International Energy and Environment Foundation.

[2]   Barbir, F. (2013). PEM fuel cells: theory and practice. Academic Press.

[3]   Larminie, J., & Dicks, A. (2003). Fuel Cell Systems Explained, 2nd edn Wiley. New York, USA.

[4]   Wang, Y., Chen, K. S., Mishler, J., Cho, S. C., & Adroher, X. C. (2011). A review of polymer electrolyte membrane fuel cells: technology, applications, and needs on fundamental research. Applied Energy, 88(4), 981-1007.

[5]   Yan, Q., Toghiani, H., Lee, Y. W., Liang, K., & Causey, H. (2006). Effect of sub-freezing temperatures on a PEM fuel cell performance, startup and fuel cell components. Journal of Power Sources, 160(2), 1242-1250.

[6]   Tsuchiya, H., & Kobayashi, O. (2004). Mass production cost of PEM fuel cell by learning curve. International Journal of Hydrogen Energy, 29(10), 985-990.

[7]   Watkins, D. S., Dircks, K. W., & Epp, D. G. (1991). U.S. Patent No. 4,988,583. Washington, DC: U.S. Patent and Trademark Office.

[8]   Li, X., & Sabir, I. (2005). Review of bipolar plates in PEM fuel cells: Flow-field designs. International Journal of Hydrogen Energy, 30(4), 359-371.

[9]   Chen, J., Siegel, J. B., Matsuura, T., & Stefanopoulou, A. G. (2011). Carbon corrosion in PEM fuel cell dead-ended anode operations. Journal of the Electrochemical Society, 158(9), B1164-B1174.

[10]   Patterson, T. W., & Darling, R. M. (2006). Damage to the cathode catalyst of a PEM fuel cell caused by localized fuel starvation. Electrochemical and Solid-State Letters, 9(4), A183-A185.

[11]   Reiser, C. A., Bregoli, L., Patterson, T. W., Jung, S. Y., Yang, J. D., Perry, M. L., & Jarvi, T. D. (2005). A reverse-current decay mechanism for fuel cells. Electrochemical and Solid-State Letters, 8(6), A273-A276.

[12]   Maharudrayya, S., Jayanti, S., & Deshpande, A. P. (2005). Flow distribution and pressure drop in parallel-channel configurations of planar fuel cells. Journal of

Power Sources, 144(1), 94-106.

[13] Kee, R. J., Korada, P., Walters, K., & Pavol, M. (2002). A generalized model of the flow distribution in channel networks of planar fuel cells. Journal of Power Sources, 109(1), 148-159.

[14] Wei, M., Fan, Y., Luo, L., & Flamant, G. (2015). CFD-based evolutionary algorithm for the realization of target fluid flow distribution among parallel channels. Chemical Engineering Research and Design, 100, 341-352.

[15] Jackson, J. M., Hupert, M. L., & Soper, S. A. (2014). Discrete geometry optimization for reducing flow non-uniformity, asymmetry, and parasitic minor loss pressure drops in Z-type configurations of fuel cells. Journal of Power Sources, 269, 274-283.

[16] Spurrier, F. R., Pierce, B. L., & Wright, M. K. (1986). U.S. Patent No. 4,631,239. Washington, DC: U.S. Patent and Trademark Office.

[17] Watkins, D. S., Dircks, K. W., & Epp, D. G. (1992). U.S. Patent No. 5,108,849. Washington, DC: U.S. Patent and Trademark Office.

[18] Rodatz, P., Büchi, F., Onder, C., & Guzzella, L. (2004). Operational aspects of a large PEFC stack under practical conditions. Journal of Power Sources, 128(2), 208-217.

[19] Zhang, J., Xie, Z., Zhang, J., Tang, Y., Song, C., Navessin, T., ... & Liu, Z. S. (2006). High temperature PEM fuel cells. Journal of Power Sources, 160(2), 872-891.

[20] Kandlikar, S. G., & Lu, Z. (2009). Fundamental research needs in combined water and thermal management within a proton exchange membrane fuel cell stack under normal and cold-start conditions. Journal of Fuel Cell Science and Technology, 6(4), 044001.

[21] Ahluwalia, R. K., & Wang, X. (2007). Buildup of nitrogen in direct hydrogen polymer-electrolyte fuel cell stacks. Journal of Power Sources, 171(1), 63-71.

[22] Faghri, A., & Guo, Z. (2005). Challenges and opportunities of thermal management issues related to fuel cell technology and modeling. International Journal of Heat and Mass Transfer, 48(19), 3891-3920.

[23] Guo, L., Zhang, G., Xu, C., Ma, L., Shen, S., Liu, H., ... & Sun, H. (2009). Study of thermal management in PEM fuel cells with numerical modeling and in situ Diagnosis approaches. In ICHMT DIGITAL LIBRARY ONLINE. Begel House Inc..

[24] Mench, M. M. (2008). Fuel cell engines. John Wiley & Sons.

[25]   Takashiba, T., & Yagawa, S. (2009). Development of fuel cell coolant. Honda R&D technical review: Honda R&D C.

[26]   Sasmito, A. P., Birgersson, E., & Mujumdar, A. S. (2011). Numerical investigation of liquid water cooling for a proton exchange membrane fuel cell stack. Heat Transfer Engineering, 32(2), 151-167.

[27]   Chen, F. C., Gao, Z., Loutfy, R. O., & Hecht, M. (2003). Analysis of optimal heat transfer in a PEM fuel cell cooling plate. Fuel Cells, 3(4), 181-188.

[28]   Choi, J., Kim, Y. H., Lee, Y., Lee, K. J., & Kim, Y. (2008). Numerical analysis on the performance of cooling plates in a PEFC. Journal of mechanical science and technology, 22(7), 1417-1425.

[29]   Bernardi, D. M., & Verbrugge, M. W. (1991). Mathematical model of a gas diffusion electrode bonded to a polymer electrolyte. AIChE journal, 37(8), 1151-1163.

[30]   Bernardi, D. M., & Verbrugge, M. W. (1992). A mathematical model of the solid-polymer-electrolyte fuel cell. Journal of the Electrochemical Society, 139(9), 2477-2491.

[31]   Costamagna, P. (2001). Transport phenomena in polymeric membrane fuel cells. Chemical engineering science, 56(2), 323-332.

[32]   Rowe, A., & Li, X. (2001). Mathematical modeling of proton exchange membrane fuel cells. Journal of power sources, 102(1), 82-96.

[33]   Springer, T. E., Zawodzinski, T. A., & Gottesfeld, S. (1991). Polymer electrolyte fuel cell model. Journal of the Electrochemical Society, 138(8), 2334-2342.

[34]   Gurau, V., Liu, H., & Kakac, S. (1998). Two-dimensional model for proton exchange membrane fuel cells. AIChE Journal, 44(11), 2410-2422.

[35]   Hum, B., & Li, X. (2004). Two-dimensional analysis of PEM fuel cells. Journal of applied electrochemistry, 34(2), 205-215.

[36]   Jung, S. Y., & Nguyen, T. V. (1998). An along-the-channel model for proton exchange membrane fuel cells. Journal of the Electrochemical Society, 145(4), 1149-1159.

[37]   Um, S., Wang, C. Y., & Chen, K. S. (2000). Computational fluid dynamics modeling of proton exchange membrane fuel cells. Journal of the Electrochemical society, 147(12), 4485-4493.

[38]   Berning, T., Lu, D. M., & Djilali, N. (2002). Three-dimensional computational analysis of transport phenomena in a PEM fuel cell. Journal of power sources,

106(1), 284-294.

[39]   Dutta, S., Shimpalee, S., & Van Zee, J. W. (2000). Three-dimensional numerical simulation of straight channel PEM fuel cells. Journal of Applied Electrochemistry, 30(2), 135-146.

[40]   Liu, H., Zhou, T., & Cheng, P. (2005). Transport phenomena analysis in proton exchange membrane fuel cells. Journal of Heat Transfer, 127(12), 1363-1379.

[41]   Mazumder, S., & Cole, J. V. (2003). Rigorous 3-D mathematical modeling of PEM fuel cells I. Model predictions without liquid water transport. Journal of the Electrochemical Society, 150(11), A1503-A1509.

[42]   Meng, H., & Wang, C. Y. (2005). Multidimensional modelling of polymer electrolyte fuel cells under a current density boundary condition. Fuel Cells, 5(4), 455-462.

[43]   Sivertsen, B. R., & Djilali, N. (2005). CFD-based modelling of proton exchange membrane fuel cells. Journal of Power Sources, 141(1), 65-78.

[44]   Nguyen, T. V., & White, R. E. (1993). A water and heat management model for Proton-Exchange-Membrane fuel cells. Journal of the Electrochemical Society, 140(8), 2178-2186.

[45]   Pasaogullari, U., Wang, C. Y., & Chen, K. S. (2005). Two-phase transport in polymer electrolyte fuel cells with bilayer cathode gas diffusion media. Journal of the Electrochemical Society, 152(8), A1574-A1582.

[46]   Weber, A. Z., & Newman, J. (2005). Effects of microporous layers in polymer electrolyte fuel cells. Journal of the Electrochemical Society, 152(4), A677-A688.

[47]   Hu, G., & Fan, J. (2006). A three-dimensional, multicomponent, two-phase model for a proton exchange membrane fuel cell with straight channels. Energy & fuels, 20(2), 738-747.

[48]   Ju, H. (2008). Analyzing the effects of immobile liquid saturation and spatial wettability variation on liquid water transport in diffusion media of polymer electrolyte fuel cells (PEFCs). Journal of Power Sources, 185(1), 55-62.

[49]   Meng, H., Han, B., & Ruan, B. (2013). Numerical modeling of liquid water transport inside and across membrane in PEM fuel cells. Asia-Pacific Journal of Chemical Engineering, 8(1), 104-114.

[50]   Siegel, N. P., Ellis, M. W., Nelson, D. J., & Von Spakovsky, M. R. (2004). A two-dimensional computational model of a PEMFC with liquid water transport. Journal of Power Sources, 128(2), 173-184.

[51]   Wang, X. D., Xu, J. L., & Lee, D. J. (2012). Parameter sensitivity examination for a complete three-dimensional, two-phase, non-isothermal model of polymer electrolyte membrane fuel cell. International journal of hydrogen energy, 37(20), 15766-15777.

[52]   Wu, H., Li, X., & Berg, P. (2009). On the modeling of water transport in polymer electrolyte membrane fuel cells. Electrochimica Acta, 54(27), 6913-6927.

[53]   You, L., & Liu, H. (2002). A two-phase flow and transport model for the cathode of PEM fuel cells. International journal of heat and mass transfer, 45(11), 2277-2287.

[54]   Hickner, M. A., Siegel, N. P., Chen, K. S., Hussey, D. S., Jacobson, D. L., & Arif, M. (2008). In situ high-resolution neutron radiography of cross-sectional liquid water profiles in proton exchange membrane fuel cells. Journal of The Electrochemical Society, 155(4), B427-B434.

[55]   Hussey, D. S., Jacobson, D. L., Arif, M., Owejan, J. P., Gagliardo, J. J., & Trabold, T. A. (2007). Neutron images of the through-plane water distribution of an operating PEM fuel cell. Journal of Power Sources, 172(1), 225-228.

[56]   Turhan, A., Heller, K., Brenizer, J. S., & Mench, M. M. (2006). Quantification of liquid water accumulation and distribution in a polymer electrolyte fuel cell using neutron imaging. Journal of Power Sources, 160(2), 1195-1203.

[57]   Kumbur, E. C., Sharp, K. V., & Mench, M. M. (2007). Validated Leverett approach for multiphase flow in PEFC diffusion media I. Hydrophobicity effect. Journal of the Electrochemical Society, 154(12), B1295-B1304.

[58]   Martínez, M. J., Shimpalee, S., Van Zee, J. W., & Sakars, A. V. (2009). Assessing methods and data for pore-size distribution of PEMFC gas-diffusion media. Journal of the Electrochemical Society, 156(5), B558-B564.

[59]   Vol'fkovich, Y. M., Sosenkin, V. E., Nikol'skaya, N. F., & Kulova, T. L. (2008). Porous structure and hydrophilic-hydrophobic properties of gas diffusion layers of the electrodes in proton-exchange membrane fuel cells. Russian Journal of Electrochemistry, 44(3), 278-285.

[60]   Gostick, J. T., Ioannidis, M. A., Fowler, M. W., & Pritzker, M. D. (2009). Wettability and capillary behavior of fibrous gas diffusion media for polymer electrolyte membrane fuel cells. Journal of Power Sources, 194(1), 433-444.

[61]   Benziger, J., Nehlsen, J., Blackwell, D., Brennan, T., & Itescu, J. (2005). Water flow in the gas diffusion layer of PEM fuel cells. Journal of Membrane Science, 261(1), 98-106.

[62]   Fairweather, J. D., Cheung, P., St-Pierre, J., & Schwartz, D. T. (2007). A microfluidic approach for measuring capillary pressure in PEMFC gas diffusion

layers. Electrochemistry Communications, 9(9), 2340-2345.

[63] Gostick, J. T., Fowler, M. W., Ioannidis, M. A., Pritzker, M. D., Volfkovich, Y. M., & Sakars, A. (2006). Capillary pressure and hydrophilic porosity in gas diffusion layers for polymer electrolyte fuel cells. Journal of Power Sources, 156(2), 375-387.

[64] Harkness, I. R., Hussain, N., Smith, L., & Sharman, J. D. B. (2009). The use of a novel water porosimeter to predict the water handling behaviour of gas diffusion media used in polymer electrolyte fuel cells. Journal of Power Sources, 193(1), 122-129.

[65] Umichedu. (2015). Umichedu. Retrieved 10 August, 2015, from http://fuelcell.engin.umich.edu/downloads/.

[66] COMSOL Multiphysics Reference Guide 5.1, 2015, COMSOL, A.B.

[67] Bird, R. B., Stewart, W. E., & Lightfoot, E. N. (2002). Transport phenomena. 2nd. New York.

[68] Voss, H. H., & Chow, C. Y. (1993). Coolant flow field plate for electrochemical fuel cells (No. US 5230966; A).

[69] Bergman, T. L., & Incropera, F. P. (2011). Introduction to heat transfer. John Wiley & Sons.

[70] Ge, S., Li, X., Yi, B., & Hsing, I. M. (2005). Absorption, desorption, and transport of water in polymer electrolyte membranes for fuel cells. Journal of the Electrochemical Society, 152(6), A1149-A1157.

[71] He, W., Yi, J. S., & Van Nguyen, T. (2000). Two-phase flow model of the cathode of PEM fuel cells using interdigitated flow fields. AIChE Journal, 46(10), 2053-2064.

[72] Nam, J. H., & Kaviany, M. (2003). Effective diffusivity and water-saturation distribution in single-and two-layer PEMFC diffusion medium. International Journal of Heat and Mass Transfer, 46(24), 4595-4611.

[73] Lin, G., He, W., & Van Nguyen, T. (2004). Modeling liquid water effects in the gas diffusion and catalyst layers of the cathode of a PEM fuel cell. Journal of the Electrochemical Society, 151(12), A1999-A2006.

[74] McKahn, D. A. (2015). Influence of gas channel depth in self-humidified miniature PEM fuel cells with dead-ended anode. International Journal of Hydrogen Energy, 40(22), 7168-7181.